

Minimalist Natural ORPphilin Macarangin B Delineates OSBP Biological Function

Gwenaëlle Jézéquel, Zoé Grimanelli, Carole Guimard, Joëlle Bigay, Juliano Haddad, Jérôme Bignon, Cécile Apel, Vincent Steinmetz, Laurie Askenatzis, Hélène Levaïque, Clara Pradelli, Van Cuong Pham, Doan T. M. Huong, Marc Litaudon, Romain Gautier, Chaker El Kalamouni, Bruno Antonny, Sandy Desrat, Bruno Mesmin,* and Fanny Roussi*



Cite This: *J. Med. Chem.* 2025, 68, 196–211



Read Online

ACCESS |



Metrics & More

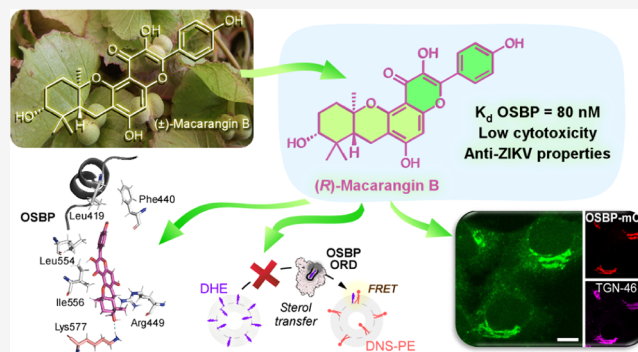


Article Recommendations



Supporting Information

ABSTRACT: OSBP ligands from the ORPphilin family are chemically complex natural products with promising anticancer properties. Here, we describe macarangin B, a natural racemic flavonoid selective for OSBP, which stands out from other ORPphilins due to its structural simplicity and distinct biological activity. Using a bioinspired strategy, we synthesized both (*R,R,R*) and (*S,S,S*)-macarangin B enantiomers, enabling us to study their interaction with OSBP based on their unique optical properties. Experimental and computational analyzes revealed that (*R,R,R*)-macarangin B has the highest affinity for OSBP. Importantly, both enantiomers showed significantly decreased cytotoxicity compared to other ORPphilins, suggesting OSBP is not the primary target in ORPphilin-induced cell death. Yet, OSBP is an attractive antiviral target, as it is hijacked by many positive-strand RNA viruses. Remarkably, (*R,R,R*)-macarangin B significantly inhibited Zika virus replication in human cells, highlighting its potential as a lead compound for antiviral drug development.



INTRODUCTION

Living organisms such as plants, marine life, and microorganisms produce specialized metabolites to defend themselves against predators or pests. These molecules kill attackers by binding to specific proteins, disrupting their metabolic processes. They exhibit precise biological activities through optimized interaction with their target, helping species survive over time. Many of these metabolites are considered promising for therapeutic use, as they can bind to their intended target (e.g., antibiotics) or to a similar human target.^{1,2} According to Waldmann and colleagues, these metabolites are privileged structures prevalent by nature.³ They often have complex structures with multiple asymmetric centers, giving them pharmacological specificity. They also show high chemical diversity and embrace a biologically relevant chemical space.⁴ However, their complexity makes them difficult to synthesize in large quantities, and their supply can be limited. Still, they remain valuable starting points for drug discovery.

In this context, four families of natural molecules with high structural complexity and lacking obvious similarity, produced either by marine organisms (cephalostatin 1,⁵ ritterazine B⁶ and stelletin E)⁷ or plants (OSW-1⁸ and schweinfurthins [SWs], like SW-G)^{5,6,9–9} were described to be highly cytotoxic and induce a similar pattern of toxicity against the NCI 60 cancer cell lines (Figure 1A). The COMPARE algorithm, which sorts drugs

according to their patterns of growth inhibitory profiles, predicted these specialized metabolites to act via a related and new mechanism of action, totally different to that of any of the chemotherapeutics already on the market.¹⁰ The only common targets identified to date for cephalostatin 1, ritterazine B, OSW-1 and SWs are oxysterol-binding protein (OSBP) and, with the exception of SWs, its closely related homologue OSBP-related protein 4 (ORP4). As a result, these compounds have been collectively termed ORPphilins.¹¹ OSBP/ORPs constitute a large and conserved family of intracellular lipid transfer proteins that mainly operate at membrane contact sites between organelles.^{12,13} In previous studies, we showed that OSBP transfers cholesterol from the endoplasmic reticulum (ER) to the trans-Golgi network (TGN) via its OSBP-related domain (ORD), by counter-exchange and hydrolysis of phosphatidylinositol-4-phosphate [PI(4)P].^{14,15} We also demonstrated that

Received: July 23, 2024

Revised: December 6, 2024

Accepted: December 12, 2024

Published: December 20, 2024



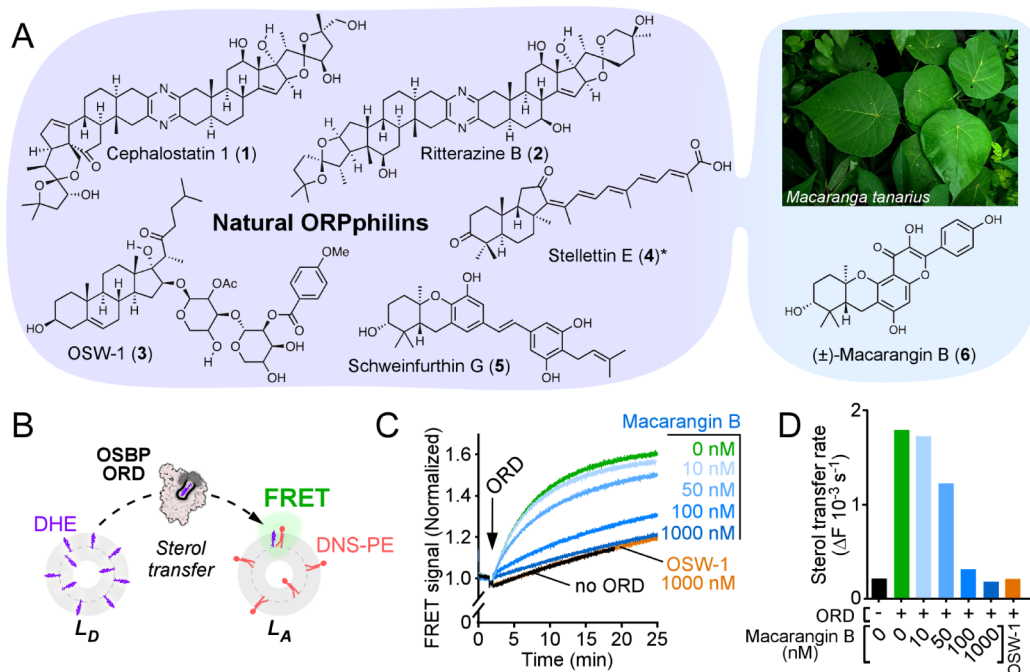


Figure 1. New ORPphilin macarangenin B (6) is a potent inhibitor of OSBP-mediated lipid transport. (A) Natural molecules already known as ORPphilins (left) and the structure of natural racemic macarangenin B (6) (right), isolated from the Vietnamese endemic plant *Macaranga tanarius* (photo by Blue Bottle, plantnet.org). Note the simplicity of macarangenin B (6) structure compared to other ORPphilins. Asterisk denotes that stelletin E was not tested by Burgett *et al.* for its potential interaction with OSBP due to limited availability.¹¹ (B) Principle of the sterol transfer assay between donor (L_D) and acceptor (L_A) liposomes catalyzed by the OSBP ORD domain, as measured by FRET between DHE and DNS-PE. (C) Time course of DHE transfer between liposomes with increasing amounts of macarangenin B (6), or as a comparison, with OSW-1 (3) (1000 nM, orange curve). Transfer was initiated by the addition of 100 nM ORD. (D) Macarangenin B (6) inhibits DHE transfer activity in a dose dependent manner.

ORPphilins like OSW-1 (3) or SW-G (5) inhibit this activity by binding directly within the ORD of OSBP.^{16,17}

Although ORPphilins have been described as highly promising anticancer agents both *in vitro* and *in vivo*, the causal relationship between their affinity for OSBP and their cytotoxicity remains elusive, as the role of OSBP in cell survival is still unclear at present.^{18,19} In line with this, certain ORPphilin-like compounds were shown to interact with potential targets other than OSBP/ORPs;²⁰ which could explain the observed cytotoxic activity. Furthermore, ORPphilin development has been hindered by their limited availability. Yet, recent studies have reported efficient total syntheses of these compounds.^{21–24}

Importantly, evidence suggests that OSBP inhibitors may help combat viral infection since the OSBP machinery is hijacked by many positive-strand RNA viruses.^{25–32} Nevertheless, all ORPphilins described so far are highly cytotoxic, compromising their use as potential antiviral drugs, and the non-natural OSBP inhibitors with antiviral potential lack selectivity toward this protein.^{27,28,30–32} Herein, we describe natural macarangenin B (6), a racemic flavonol carrying an uncommon hydroxy-hexahydroxanthene (HHX) moiety that we isolated from *Macaranga tanarius*, an endemic plant species from Vietnam. We demonstrated that this hydroxy-HHX confers the ability to bind OSBP selectively and dissected the specific interaction of both macarangenin B (6) synthetic enantiomers with OSBP using molecular dynamics (MD) simulations, biochemical and cellular approaches. This selectivity indicates that the main targets involved in ORPphilin-induced cell death mechanisms are not OSBP/ORP4. Building on this, we have validated OSBP as a relevant antiviral target.

RESULTS

Isolation of (±)-Macarangenin B (6) and Bioinspired Synthesis of Both Enantiomers.

A few years ago, we reported the isolation of SW derivatives from a *Macaranga tanarius* crude extract.^{33–35} From the same extract, we isolated and characterized an original flavonol 6 possessing a similar HHX unit as SWs (Figure 1A and Supporting Information). This compound was isolated at 2 mg scale with a very low extraction yield (0.00017%). Of note, flavonoids represent one of the most widespread classes of specialized metabolites produced throughout the plant kingdom.³⁶ Of these, some 1,000 prenylated flavonoids are regarded as phytoalexins.³⁷ Although some previously isolated molecules of the ugonin family carry a *cis*-HHX unit,^{38,39} the hydroxylated *trans*-HHX unit found in compound 6 has never been described before. Given the presence of this particular SW-like *trans*-HHX motif specific to the *Macaranga* genus, we surmised that macarangenin B (6) could be a new ORPphilin, in which case it would be the simplest of the family. We thus examined whether compound 6 could inhibit the cholesterol transfer activity of OSBP, as previously observed with OSW1 (3) and SW-G (5).^{16,17} For this, we monitored the transfer of the cholesterol fluorescent analog dehydroergosterol (DHE) by OSBP ORD from liposomes mimicking the ER to liposomes mimicking the TGN (Figure 1B). The DHE transfer rate decreased drastically as we increased the concentration of macarangenin B (6) (Figure 1C,D), suggesting that it binds to the ORD domain of OSBP with a high affinity and can therefore be considered an ORPphilin.

Unlike SW derivatives with a hydroxy-HHX motif, compound 6 was isolated as a racemate (specific rotation and ECD in Supporting Information). It has been shown, however, that

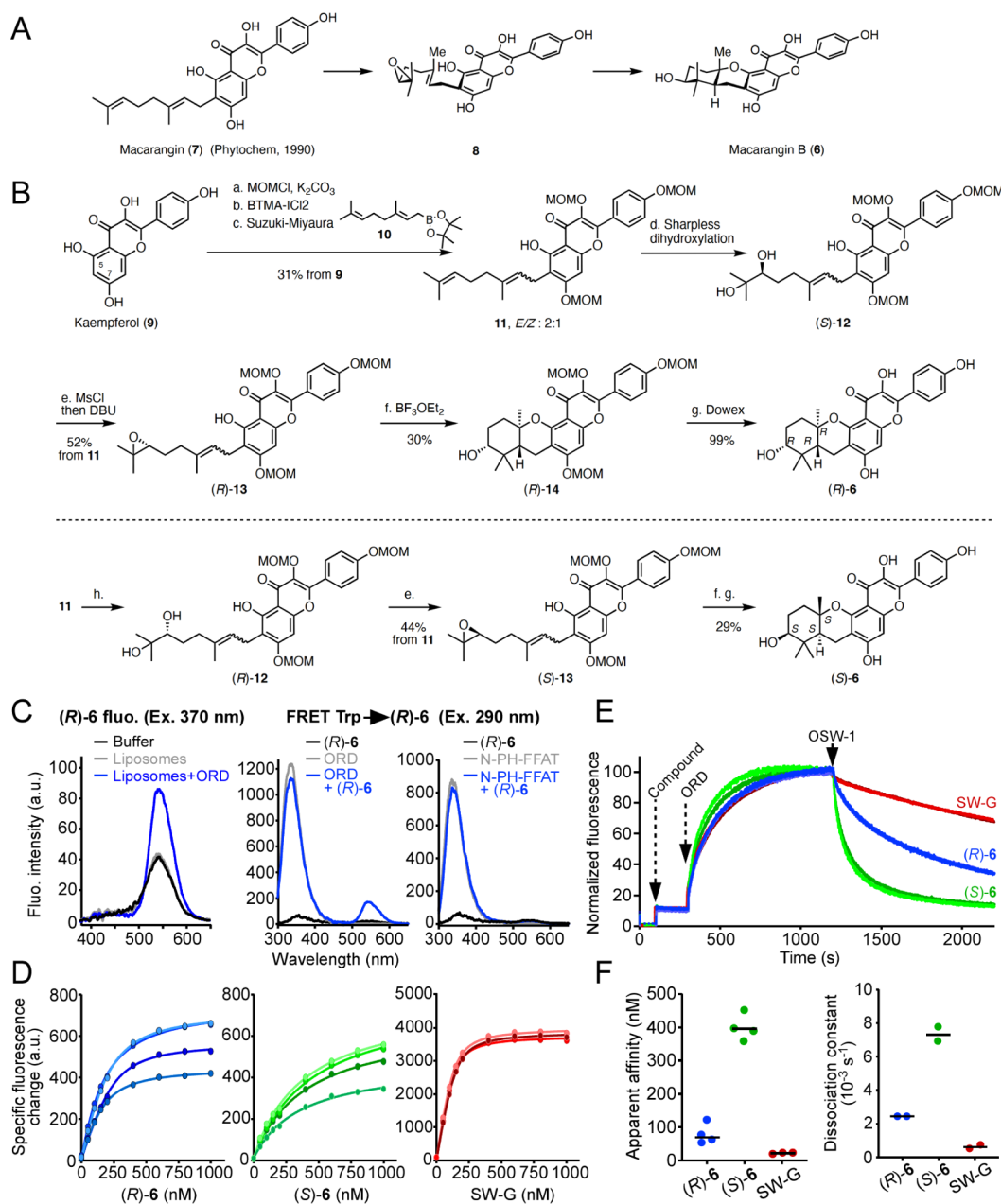


Figure 2. Bioinspired enantioselective synthesis of macarangenin B (*R*)-6 and (*S*)-6 in seven steps from kaempferol (9) and their interaction with OSBP. (A) Biogenetic proposal for macarangenin B (6). (B) Reaction conditions: (a) K_2CO_3 (12.0 equiv), MeCN/DMSO 10:1, 40 °C, 1 h, then dropwise addition (1 h) of MOMCl (5.0 equiv), room temperature (r.t.), 16 h; (b) $NaHCO_3$ (5.0 equiv), BTMA- ICl_2 (1.05 equiv), CH_2Cl_2 /MeOH 2:1, dark, r.t., 1 h; (c) boronic ester 10 (1.5 equiv), NaOH (2.5 equiv), $Pd(PPh_3)_4$ (2 mol %), degassed THF/water 2:1, microwave irradiation, 100 °C, 4 h; (d) K_2CO_3 (4.0 equiv), K_3FeCN_6 (2.8 equiv), (DHQD)₂PHAL (4 mol %), OsO_4 (4 mol %), $MeSO_2NH_2$ (1.3 equiv), *t*-BuOH/water 2:1, 0 °C, 16 h; (e) Et_3N (4.0 equiv), $MeSO_2Cl$ (2.0 equiv), r.t., 1 h, then DBU (5.0 equiv), 0 °C, 3 h; (f) $BF_3 \cdot OEt_2$ (1.5 equiv), CH_2Cl_2 , −78 °C, 30 min; (g) Dowex 50WX8 200–400 (15.0 equiv), MeOH, 35 °C, 22 h; (h) same as (d) but (DHQD)₂PHAL instead of (DHQD)₂PHAL. (C) Emission spectra of (*R*)-6 (200 nM) upon excitation at 370 nm in HKM buffer, or in the presence of PC liposomes (100 μ M), with or without ORD (200 nM) in HKM buffer (left panel). Emission spectra of (*R*)-6 (200 nM) upon FRET excitation at 290 nm in the presence of PC liposomes (100 μ M) with or without ORD (200 nM) (middle panel) or N-PH-FFAT (200 nM) (right panel) in HKM buffer. (D) Binding measurements of (*R*)-6 (left panel), (*S*)-6 (middle panel) or SW-G (right panel) to ORD under FRET conditions. Increasing amounts of compounds were added in HKM buffer containing Thesit (0.02%) in the presence of ORD (200 nM). The graphs represent corrected fluorescence increase after deduction of compound fluorescence increase obtained without ORD at the same concentration, as shown in Figure S1H. (*R*)-6 and SW-G curves were fitted with quadratic equation and (*S*)-6 curves were fitted with hyperbolic equation. Color shades are independent experiments. (E) Time course of (*R*)-6, (*S*)-6 and SW-G (200 nM) (blue, green and red curves, respectively) binding to the ORD (200 nM), and release upon OSW-1 addition (500 nM) as measured by FRET ((*R*)-6 and (*S*)-6: Ex. 290 nm, Em. 550 nm; SW-G: Ex. 280 nm, Em. 410 nm). The reaction was performed in the presence of PC liposomes (100 μ M). Maximum fluorescence intensity was normalized to 100 for comparison between the three compounds. (F) Fitting the curves shown in D allows determination of (*R*)-6, (*S*)-6 and SW-G K_d for ORD (left panel). Dissociation constants (k_{off}) after OSW-1 addition were determined by mono exponential fitting of the curves in E (right panel).

chirality plays an important role in the mode of action of SWs: unnatural (*S,S,S*) enantiomers show a distinctive pattern of activity on the NCI 60 cell lines panel compared to their natural (*R,R,R*) counterparts,⁴⁰ suggesting that the two-enantiomer series may differ in their mechanisms of action. To verify this hypothesis and because the racemate was isolated at a small scale, we sought to carry out the synthesis of both (*R,R,R*) and (*S,S,S*) enantiomers of macarangenin B (**6**), i.e., (*R*)-**6** and (*S*)-**6** respectively (Figure 2), following a bioinspired strategy.

From a biogenetic point of view, the hydroxy-HHX moiety is proposed to arise from the intramolecular “head-to-tail” polyene cyclization of a phenol on an epoxidized geranyl side chain (Figure 2A).⁴¹ This highly efficient reaction is one of the finest means used by living organisms to create complex polycyclic molecules from acyclic ones via concerted and stereocontrolled C–C bond formations. Thus, the possible biosynthetic precursor of compound **6** is macarangenin (**7**), which has already been isolated from *Macaranga vedeliana* (Figure 2A).⁴² In this process, the geranyl chain of **7** is subjected to nonenzymatic epoxidation to form intermediate **8**. By contrast, the intramolecular cyclization to the HHX moiety is likely enzymatic as it originates from the less reactive phenol of **8** involved in a hydrogen bond with the adjacent ketone.

Macarangenin (**7**) has been synthesized in six steps with an overall yield of 6%, following the classic strategy of forming the flavone skeleton at the end of the synthesis.⁴³ Here, we have chosen a shorter, bioinspired strategy to synthesize macarangenin B (**6**), starting from commercial kaempferol (**9**), the probable biogenetic precursor of **6** and **7**, and using a Suzuki–Miyaura coupling reaction to introduce the geranyl chain (Figure 2B). For that, the phenol functions of kaempferol (**9**) were first protected as methoxymethyl acetal, except the poorly reactive phenol on C₅ engaged in an intramolecular hydrogen bond with the carbonyl moiety. This free phenol was then used to direct regioselective iodination on C₆ in the presence of benzyltrimethylammonium dichloriodate (BTMA-ICl₂).^{44,45} The iodinated intermediate was obtained with a good regioselectivity of 7:1 in favor of the functionalization of C₆ versus C₈ position. The next step consisted in introducing the geranyl chain by a Suzuki–Miyaura coupling using geranyl boronic acid pinacol ester **10**.⁴⁶ The choice of appropriate solvents and base turned out to be crucial. The optimal conditions finally involved the use of Pd(PPh₃)₄ as a catalyst along with NaOH as a base in a mixture of THF/water 1:1 at 100 °C under microwave irradiation for 4 h. With these conditions, the desired coupling product **11** was obtained in 60% yield over two steps and in 31% yield from kaempferol (**9**). However, this reaction was accompanied by partial isomerization of the *E* allylic double bond (*E/Z* 2:1). None of the tested catalysts (PdCl₂(dppf), Pd(PPh₃)₂Cl₂) or conditions (use of K₂CO₃, KOtBu, K₃PO₄, CsF, Cs₂CO₃ in DMF, THF or dioxane at temperatures ranging from 50 to 90 °C) could prevent or reduce this side reaction.

When performing direct enantioselective epoxidation of the terminal double bond of compound **11** following Shi or Jacobsen strategies, we observed a lack of chiral induction, regioselectivity and/or very low yield. The desired epoxides (*R*)-**13** and (*S*)-**13** were thus prepared by dihydroxylation followed by cyclization. First, a Sharpless dihydroxylation was carried out in the presence of (DHQD)₂PHAL or (DHQD)₂PHAL to afford (*S*)-**12** and (*R*)-**12**, respectively. After mesylation of the secondary alcohol obtained, the use of DBU afforded the desired epoxides (*R*)-**13** and (*S*)-**13** with 52% and 44% yield, respectively from geranyl intermediate **11**. The hydroxy-HHX

moiety was then obtained by a cascade cyclization induced by a Lewis acid. The use of a stoichiometric amount of BF₃·OEt₂ in dichloromethane at –78 °C afforded the cyclized compounds (*R,R,R*)-**14**, i.e. (*R*)-**14** and (*S,S,S*)-**14**, i.e. (*S*)-**14**. Both could be easily separated from their respective diastereomers arising from the cyclization of (*R,Z*)-**13** and (*S,Z*)-**13** (see Supporting Information). The two enantiomers of protected macarangenin B (*R*)-**14** and (*S*)-**14** were obtained with good enantiomeric ratios (*e.r.*) of 90:10 and 97:3, respectively (see Supporting Information). Gentle deprotection of the phenols using Dowex acidic resin 50WX8 200–400 in methanol at 35 °C for 22 h yielded the two enantiomers of macarangenin B (*R*)-**6** and (*S*)-**6** quantitatively. By contrast, classical deprotection with 2 M HCl or *p*-toluenesulfonic acid led to complete degradation. Spectroscopic data (¹H and ¹³C NMR) and mass spectra of (*R*)-**6** and (*S*)-**6** were identical to those of isolated natural macarangenin B (**6**). All compounds are >95% pure by HPLC.

Intrinsic Fluorescence of Macarangenin B Enantiomers Reveals Preferential Binding of (*R*)-6** to OSBP.** We noticed that macarangenin B (**6**) enantiomers exhibit intrinsic fluorescence with excitation and emission spectra in the UV–visible range (Figure S1A,B), as described for other flavonols,^{47,48} with two excitation peaks at 280 and 370 nm and two emission peaks at 475 and 550 nm. Interestingly, spectral data analysis revealed high sensitivity to the environment (Figure S1D,E), hinting that their binding to the ORD hydrophobic pocket could be readily detectable by fluorescence change, as previously observed with SW-G (**5**).¹⁷ Our results indicated that (*R*)-**6** and (*S*)-**6** emission peaks at 550 nm strongly increased upon ORD addition (Figure 2C, left panel, and Figure S1E), suggesting that both compounds enter into the ORD of OSBP. To confirm the specific binding of compounds **6** to ORD, we sought to perform fluorescence resonance energy transfer (FRET) experiments: according to the crystal structure of the OSBP ORD (PDB: 7 V62), tryptophan residues located in the vicinity of the lipid-binding cavity should be close enough to inserted macarangenin B (**6**) to form fluorophore pairs, resulting in a FRET signal (Figure S1F). We thus compared the emission spectra of the ORD alone, of compounds (*R*)- or (*S*)-**6** alone, and of mixtures containing stoichiometric amounts of both ORD and (*R*)- or (*S*)-**6** upon Trp excitation at 290 nm. As shown in Figures 2C and S1G, the emission signal at 550 nm of (*R*)- or (*S*)-**6** had a ~10-fold higher intensity in the presence of ORD (colored curves) as compared to (*R*)- or (*S*)-**6** alone. As a control, we performed the same experiments with the membrane tethering region of OSBP (N-PH-FFAT; res. 1–408). Under these conditions, no FRET was observed. These experiments demonstrated that both (*R*)- and (*S*)-**6** molecules bind specifically to the ORD of OSBP.

We next used this FRET signal to assess the affinity of both macarangenin B (**6**) enantiomers for the ORD. The increase in signal when adding incremental amount of each compound was measured both with and without the ORD (Figure S1H). Plotting the specific FRET signal for (*R*)- and (*S*)-**6** against compound concentration enabled determination of their apparent affinity (*K_d*) for ORD (Figure 2D). Strikingly, the affinity of (*R*)-**6** (*K_d* = 80 ± 30 nM) for ORD was five times higher than that of (*S*)-**6** (*K_d* = 401 ± 38 nM) (Figure 2F, left panel). This difference is likely significant for structurally related compounds, given the ability of ORD to bind to a wide range of structurally diverse compounds and lipids. For comparison, a similar experiment was performed with SW-G (**5**) but at a different emission wavelength, showing a *K_d* = 22 ± 2 nM. We then monitored the time course of (*R*)-**6**, (*S*)-**6** and SW-G

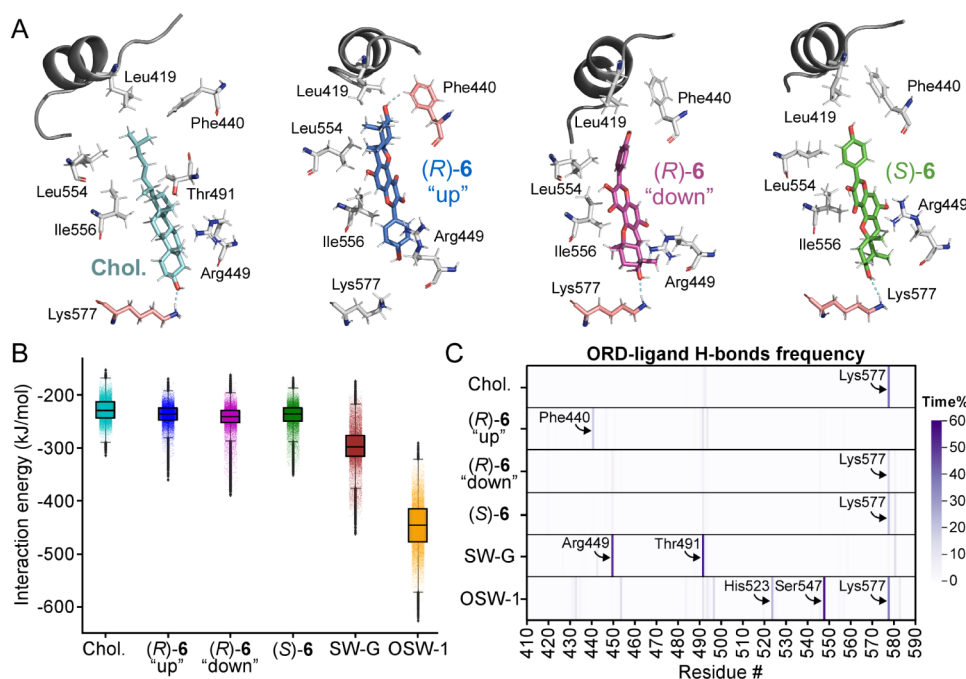


Figure 3. MD simulations of macarangan B (**6**) enantiomers. (A) MD simulations of cholesterol, (R)-**6** and (S)-**6** in OSBP ORD domain (PDB ID: 7 V62). Images are the most representative conformations of cholesterol, (R)-**6** "up", (R)-**6** "down" and (S)-**6** in the ORD pocket, as obtained from clustering the simulations of each compound. Residues that frequently form H-bonds with ligands are colored in pink. Conformations of SW-G and OSW-1 in the ORD pocket are shown in Figure S3A. (B) Interaction energy between ligands and the ORD. One point represents one simulation frame. (C) H-bond frequency between the indicated ligands and ORD residues, expressed in percentage of simulation time. Results are averaged over three replicates of 500 ns simulation for each complex.

binding into the ORD by FRET, as well as their dissociation constants (k_{off}) upon competition with an excess of OSW-1, which is not fluorescent (Figure 2E). Association kinetics were similar, probably because of the rate-limiting dissociation of the initially bound cholesterol, whereas dissociation kinetics of (R)-**6** ($k_{\text{off}} = 24 \times 10^{-4} \text{ s}^{-1}$) was three times slower than that of (S)-**6** ($k_{\text{off}} = 73 \times 10^{-4} \text{ s}^{-1}$), but faster than that of SW-G (**5**) ($k_{\text{off}} = 6 \times 10^{-4} \text{ s}^{-1}$) (Figure 2F, right panel). Although less pronounced, the relative differences in k_{off} of (R)-**6** and (S)-**6** align with those observed in K_d . We also performed gel filtration chromatography to confirm the formation of complexes between ORD and (R)-**6** or (S)-**6** by an orthogonal method (Figure S2). Consistently, these results showed different abilities of (R)-**6** or (S)-**6** to interact with ORD. Overall, these experiments demonstrate that both macarangan B (**6**) enantiomers are capable of entering the ORD pocket, but with contrasting affinities, with ORD showing preferential binding to (R)-**6**.

Molecular Dynamics Simulations Suggest That Macarangan B (R)-6** and (S)-**6** Adopt Different Orientations in OSBP.** To gain a better understanding of the selectivity of macarangan B (**6**) enantiomers for OSBP, we sought to investigate their interaction at the structural level using computational approaches. Docking simulations were performed with (R)-**6**, (S)-**6**, SW-G (**5**), OSW-1 (**3**) and cholesterol as a control. In agreement with the OSBP:cholesterol crystal structure,⁴⁹ the hydroxyl group of cholesterol was oriented toward the bottom of the ORD cavity, as was that of the SW-G HHX moiety, consistent with previous SAR studies.⁹ We found that the HHX of (S)-**6** was similarly oriented. Unexpectedly, two large clusters of low-energy binding poses were obtained for compound (R)-**6**, showing two possible orientations ("up" and "down") within the ORD pocket. For each ligand, the pose conformations with the most favorable

binding energy values were then used to perform all-atom molecular dynamics (MD) simulations (Figures 3A and S3A). All compounds remained in the OSBP ORD binding pocket throughout the simulations. Estimation of the interaction energies indicated similar stability of cholesterol, (R)-**6** and (S)-**6** within the ORD (Figure 3B). Conversely, root-mean-square fluctuation (RMSF) measurements showed that both macarangan B (**6**) enantiomers enhanced lid stability (aa. 415–451) compared to cholesterol during simulation (Figure S3B,C). Interestingly, no significant difference was found between interaction energy values for (R)-**6** "up" and "down" orientations, suggesting that there is no conformational preference for (R)-**6** within the ORD pocket (Figure 2B). Our data also confirmed that SW-G (**5**) and especially OSW-1 (**3**) form highly stable complexes with OSBP ORD.

We further analyzed the formation of hydrogen bonds (H-bonds) between each molecule and the ORD as well as their occupancy during simulations (Figure 2C). H-bonds frequently occurred between Lys577 and cholesterol (38.8% of the simulation time), (R)-**6** "down" (14.9%) and (S)-**6** (20.8%), whereas (R)-**6** "up" was involved in an OH– π H-bonding with the aromatic ring of Phe440 (18.4%) (Figure 2A,C, Movies S1–S3). In comparison, SW-G and OSW-1 formed two, three or even more H-bonds with ORD residues, with much higher frequency (up to 56.2% of the time between OSW-1 and Ser547), thereby explaining their stronger interaction with the ORD.

Taken together, our results suggest that macarangan B (**6**) enantiomers associate differentially with the ORD of OSBP at the structural level, (R)-**6** being able to take two different orientations, and that H-bonds likely maintain these compounds in the pocket. In our model, a compound with two binding modes of equal interaction energies, such as (R)-**6** (but not (S)-

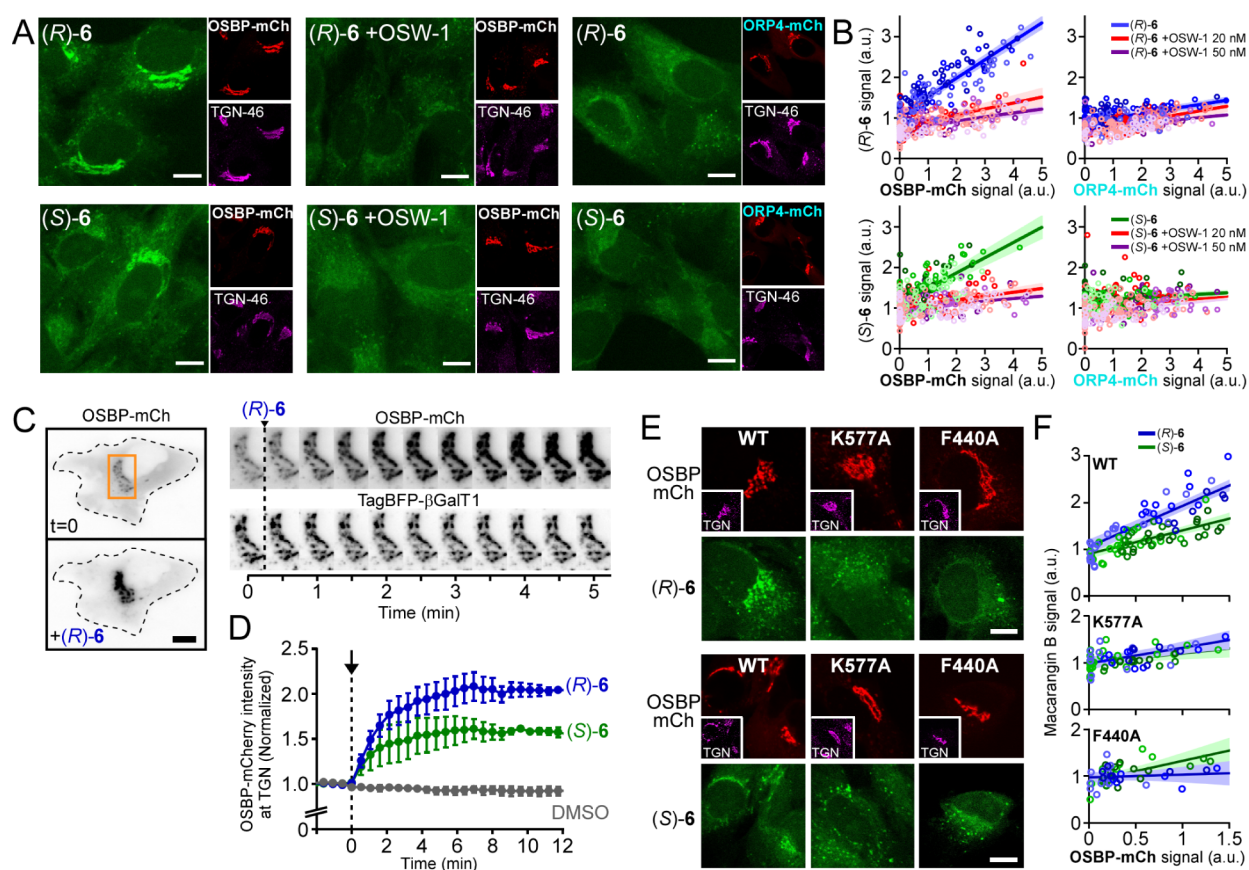


Figure 4. Direct subcellular imaging of macarangin B enantiomers (R)-6 and (S)-6. (A) Confocal images of RPE-1 transfected with OSBP-mCherry for 18 h, labeled with either (R)-6 or (S)-6 (2 μ M) for 30 min in the presence of DMSO (left panels) or OSW-1 (20 nM, middle panels), then fixed, permeabilized and immunolabeled with anti-TGN-46 antibody and a secondary antibody coupled to Alexa Fluor 647. In the right panels, cells were transfected with ORP4-mCherry instead of OSBP-mCherry. Scale bars: 10 μ m. Acquisition settings were (Ex./Em.): (R)-6 or (S)-6, 405/508–552 nm; mCherry, 561/579–632 nm; Alexa Fluor 647, 633/650–695 nm. (B) (R)-6 (top panels) or (S)-6 (bottom panels) fluorescence intensity at the TGN as a function of OSBP-mCherry or ORP4-mCherry expression levels in the presence of the indicated amount of OSW-1. Measurements were performed on 125–160 cells for each condition. Curves and shaded area are mean \pm SE of linear fits from 3 independent experiments. (C) Time-lapse microscopy of RPE-1 cells cotransfected with OSBP-mCherry and the TGN marker TagBFP- β GalT1 for 18 h and treated with (R)-6 (500 nM). Individual frames from a time series featuring the TGN area of the cell (orange box) are shown. Upon (R)-6 addition, OSBP rapidly concentrates to β GalT1-positive perinuclear regions. Scale bar: 10 μ m. (D) Normalized intensity of OSBP-mCherry at the TGN. The arrow indicates the addition of compounds, or DMSO as control, to the extracellular medium. Curves are mean \pm SE of 3 independent experiments with 14 to 18 kinetics each. (E) Confocal images of RPE-1 cells transfected with OSBP-mCherry WT, K577A or F440A, labeled and treated as in A. Scale bar: 10 μ m. (F) Quantification of (R)-6 (blue) and (S)-6 (green) fluorescence intensity at the TGN as a function of the expression level of the indicated OSBP-mCherry constructs. Measurements were performed on 30–56 cells for each condition. Curves and shaded area show mean \pm SE of linear fits from 3 independent experiments.

6), would have a higher probability of encountering the target binding site, as it can approach from various angles or positions, leading to increased affinity, in agreement with our FRET measurements.

Direct Imaging of Macarangin B (R)-6 and (S)-6 Shows Their Specific Interaction with OSBP in Cells. We next took advantage of the fluorescence properties of (R)-6 and (S)-6 to directly visualize them in a cellular context using confocal microscopy (Figure 4A). hTERT-RPE-1 cells (hereafter RPE-1) were transiently transfected with OSBP-mCherry and then treated with (R)-6 or (S)-6 (2 μ M) for 30 min at 37 $^{\circ}$ C. Strikingly, both compounds colocalized well with OSBP-mCherry and the TGN marker TGN-46. Moreover, (R)-6 and (S)-6 fluorescence level at the TGN perfectly correlated with that of OSBP-mCherry (Figure 4B), suggesting that their cellular incorporation largely depends on OSBP. We also noticed that compound (S)-6 accumulated slightly less at the TGN than (R)-6, in good agreement with their respective K_d

(Figure 2F). Interestingly, cotreatment with the nonfluorescent compound OSW-1 (3) prevented TGN labeling by (R)- or (S)-6 (Figure 4A, middle panel, and Figure 4B), indicating competition between these compounds (to the advantage of OSW-1) to bind OSBP. We also transfected RPE-1 cells with ORP4-mCherry to determine whether macarangin B (6) enantiomers can bind ORP4, the closest ortholog of OSBP,¹¹ as do most ORPphilins. Our results indicated that ORP4 overexpression did not help recruit (R)-6 or (S)-6 to TGN (Figure 4A,B, right panels), thus demonstrating that these compounds prefer to interact with OSBP.

We have previously reported that OSBP inhibition by OSW-1 (3) and SW-G (5) caused rapid increase of PI(4)P levels at the TGN, ultimately leading to massive recruitment of OSBP to the perinuclear region.¹⁶ As expected, upon (R)-6 treatment, OSBP-mCherry rapidly relocated to the TGN, marked by TagBFP- β GalT1 ($t_{1/2}$ = 1.28 min), suggesting that (R)-6 crosses cell membranes very quickly to reach OSBP (Figure 4C,D). This

Table 1. Cytotoxicity on a Panel of Eight Cell Lines of (R)- and (S)-6 Compared to SW-G and OSW1

Cell lines	(R)-6 IC ₅₀ (μM) ^a	(S)-6 IC ₅₀ (μM) ^a	SW-G IC ₅₀ (μM) ^a	OSW-1 IC ₅₀ (μM) ^a
U87-MG	2.3 ± 0.4	7.9 ± 0.3	0.008 ± 4.2 × 10 ⁻⁴	6 × 10 ⁻⁵ ± 4 × 10 ⁻⁶
A549	6.3 ± 0.02	>15	0.5 ± 0.1	1.5 × 10 ⁻⁴ ± 7 × 10 ⁻⁶
MDAMB231	7.9 ± 1.4	7.7 ± 1.8	0.3 ± 0.02	1 × 10 ⁻⁴ ± 6 × 10 ⁻⁶
MCF7	6.7 ± 1.2	6.4 ± 0.6	1.0 ± 0.04	8.4 × 10 ⁻⁴ ± 2 × 10 ⁻⁵
PC3	6.1 ± 0.06	10.8 ± 0.5	0.3 ± 0.04	2.7 × 10 ⁻⁴ ± 5 × 10 ⁻⁴
RPE1	4.9 ± 0.05	7.2 ± 0.2	0.4 ± 0.003	ND
MRC5	7.0 ± 0.2	9.3 ± 1.1	0.3 ± 0.08	ND
HeLa	6.1 ± 0.4	>15	0.1 ± 0.005	ND

^aIC₅₀ measures the drug concentration required for the inhibition of 50% cell proliferation after 72 h of incubation. It was calculated from three independent experiments in which ten different concentrations of compound ranging from 5 × 10⁻⁴ to 50 μM were used. ND: not determined.

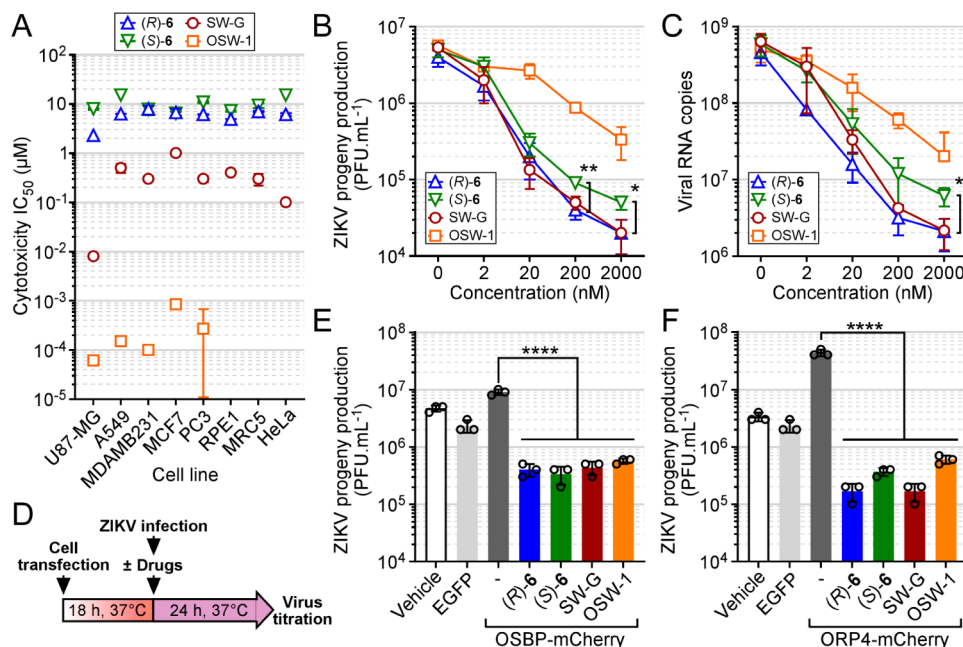


Figure 5. (R)-6 and (S)-6 show low cytotoxicity and prevent cellular infection by epidemic strain of ZIKV. (A) Cytotoxicity of (R)-6 and (S)-6 compared to that of SW-G and OSW-1 on a panel of eight cell lines. Data represent means ± SD from three independent experiments. (B) A549 cells were infected with ZIKV (PF-25013-18) at MOI of 2 and continuously incubated with increasing concentrations (0–2000 nM) of (R)-6, (S)-6, SW-G or OSW-1. ZIKV progeny production was quantified by plaque-forming assay. Unpaired *t* test between (R)-6 and (S)-6 (***p* < 0.01; **p* < 0.05). (C) Same experiment as B but in this case the amount of viral genomic RNA in ZIKV-infected cells was determined by RT-qPCR. Data represent means ± SD from three independent experiments. Unpaired *t* test between (R)-6 and (S)-6 (**p* < 0.05). (D) Protocol for synchronized cell transfection followed by ZIKV infection and drug treatment. (E) A549 cells were transfected with EGFP alone (light gray) or OSBP-mCherry. Eighteen h post-transfection, drugs (20 μM, colored bars) or DMSO (dark gray) were used for treatment throughout the infection. 24 h postinfection, the virus titer was evaluated by plaque forming assay. Data represent the means ± SD from three independent experiments. One-way ANOVA and Dunnett's test (*****p* < 0.001). (F) Same as E with ORP4-mCherry instead of OSBP-mCherry.

was confirmed by direct imaging of (R)-6 alongside OSBP at the TGN as early as 1 min after its addition to the extracellular medium (Figure S4). (S)-6 addition also caused a rapid shift (*t*_{1/2} = 1.11 min) of the OSBP pool toward the TGN, except that OSBP-mCherry fluorescence level at the TGN was significantly lower in this case (1.6- and 2.1-fold increase, respectively with (S)-6 and (R)-6) (Figure 4D).

We next sought to experimentally test the contribution of the H-bonding residues Lys577 and Phe440 (described in Figure 3C), in the interaction between OSBP and macarangan B (6) enantiomers. Cells were transfected with OSBP-mCherry constructs containing or not the point mutations K577A or F440A, and the fluorescence distribution of (R)- or (S)-6 was analyzed by imaging upon treatment as in Figure 4A. We showed that both mutations strongly reduced the ability of (R)- and (S)-6 to codistribute with OSBP in the TGN region (Figure 4E,F),

indicating that these residues play a significant role in these interactions. Although *in silico* analysis predicted that F440 formed a H-bond only with (R)-6, the F440A mutation also interfered with (S)-6 and SW-G binding to a significant extent (Figures 4E,F and S5A,B), suggesting that F440 also promotes hydrophobic interactions with these ligands.

Taken together, these experiments demonstrate that both macarangan B (6) enantiomers act directly on OSBP but not on ORP4 in cells, and that compound (R)-6, which has enhanced affinity for OSBP, concentrates in the perinuclear region and impacts OSBP dynamics more strongly than (S)-6. Moreover, residues showing to form H-bonds with the compounds *in silico* play a key role in OSBP-macarangan B (6) interaction in cells.

Macarangan B (R)-6 and (S)-6 Have Biological Activities Distinct from Those of Other ORPphilsins. Having established that macarangan B (6) is a new ORPphilsin selective

for OSBP, we compared its biological activity with that of SW-G (5) and OSW-1 (3), as the role played by this protein in their mechanism of action is not perfectly understood. All ORPphilins show a distinctive cytotoxicity profile on the NCI-60 cancer cell line screen, with highly sensitive cell lines (e.g., nanomolar cytotoxicity on CNS cancer cells) and low-responsive ones (e.g., micromolar cytotoxicity on lung cancer cells). In addition, cell sensitivity to ORPphilins was correlated with OSBP expression level: cell lines with high amounts of endogenous OSBP, or overexpressing OSBP, were more resistant to ORPphilin treatment, suggesting a titration effect.^{11,17} We used a panel of eight cell lines to assess (R)- and (S)-6 cytotoxicity, which was compared to that of SW-G (5) and OSW-1 (3) (Table 1 and Figure 5A). Strikingly, (R)-6 and (S)-6 showed cytotoxicity in the micromolar range, significantly lower than that measured with 3 and 5. Surprisingly, however, the stereochemistry of the HHX moiety had little impact on cytotoxicity, as (R)-6 and (S)-6 showed roughly the same IC_{50} on all cell lines, contrasting with their distinct affinities for OSBP. Of note, the activity pattern of unnatural (S,S,S) enantiomer of SW-F was shown to correlate poorly with that of natural (R,R,R)-series on the NCI-60 cell lines.⁴⁰ Furthermore, we could highlight a strong decorrelation between OSBP affinity and cytotoxicity, particularly on U87-MG: (R)-6 was 300 times less cytotoxic than SW-G while its affinity for OSBP is reduced only 4-fold (Table 1, Figures 2F and 5A). This difference in cytotoxicity is unlikely to be due to cell penetration issues, as indicated by our live cell imaging experiments (Figure S4), and suggests instead that the SW-G-mediated cell death pathway is independent of OSBP.

We then took advantage of the remarkably low cytotoxicity of (R)-6 and (S)-6 compared with other ORPphilins to evaluate their antiviral activities. OSBP was previously shown to play an essential role in the growth of a number of positive single-stranded RNA viruses, notably from the *Flaviviridae* and *Picornaviridae* families, by promoting the biogenesis of organelle-like structures, which serve as platforms for the viral replication machinery.^{29,49} Interestingly, OSW-1 (3) was shown to potentially inhibit the replication of various enteroviruses;⁵⁰ however, its high cytotoxicity likely hinders its application as an antiviral. We therefore examined whether (R)- and (S)-6 could inhibit *Orthoflavivirus zikaense* (Zika virus, ZIKV) growth, compared with SW-G (5) and OSW1 (3). For this, A549 cells were infected with the French Polynesia 2013 epidemic strain and incubated 24 h with increasing doses of each compound up to 2 μ M, a concentration showing no toxicity to host cells (Figure S6A). We observed that at 200 nM, SW-G, (R)- and (S)-6 reduced extracellular viral progeny production by 2 decimal logs (\log_{10}), whereas OSW-1 showed much weaker antiviral activity (Figure 5B). We next determined whether the anti-ZIKV effect was attributable to a decrease in viral RNA replication. As shown in Figure 5C, all inhibitors induced a dramatic reduction in RNA production, as measured by RT-qPCR, suggesting that these compounds act at late stages of viral infection. Nevertheless, they showed notable differences in activity: 20 nM of SW-G, (R)-6 and (S)-6 were sufficient to reduce the amount of viral RNA in ZIKV-infected A549 cells by at least 2 \log_{10} s, whereas a 100-fold higher concentration of OSW-1 (2 μ M) was required to achieve similar inhibition. Furthermore, (R)-6 and SW-G were more effective in suppressing viral RNA production in ZIKV-infected cells than (S)-6.^{28,48,49}

To determine whether the higher activity of (R)-6 and SW-G was related to their higher affinity for OSBP, cells were

transfected either with OSBP-mCherry or ORP4-mCherry before infection with ZIKV (Figures 5D and S6B). As expected, overexpressing OSBP-mCherry attenuated the antiviral activity of (R)-6, (S)-6, SW-G and OSW-1, most likely due to the titration effect mentioned before (Figure 5E). In this case, all four compounds decreased the viral titer similarly by only $\sim 1.5 \log_{10}$ s compared with untreated cells, whereas a decrease of up to 2.5 \log_{10} s was obtained without OSBP overexpression (Figure 5B). We then performed the same analyses with ZIKV-infected cells transfected with ORP4-mCherry (Figure 5F). Surprisingly, upon ORP4-mCherry overexpression viral growth increased by one \log_{10} as compared to nontransfected cells or cells transfected with an EGFP-expressing plasmid. Nevertheless, virus progeny production was strongly reduced by up to 2.4 \log_{10} s in the presence of (R)-6 and SW-G, and by 2 \log_{10} s with (S)-6. This reduction was less pronounced with OSW-1, reflecting its weaker antiviral effect, as seen in Figure 4B, and probably because both OSBP and ORP4 titrate OSW-1, resulting in less inhibition when ORP4 is overexpressed.

Taken together, these results demonstrate that (R)-6 couples its specificity toward OSBP to strong anti-ZIKV activity. Given its straightforward synthesis and its low cytotoxicity, we consider macarangin B (R)-6 to be a promising antiviral agent.

DISCUSSION

In this study, we describe the characterization of natural macarangin B (6) as a new ORPphilin, i.e., a natural compound able to bind OSBP (Figure 1). This compound is a flavonol with a rare hydroxy-HHX moiety that confers its specificity. Since it was isolated at a very small scale, and considering that the absolute configuration of the HHX motif may influence its affinity for OSBP,⁴⁰ we performed the asymmetric synthesis of the two enantiomers (R,R,R) and (S,S,S) of macarangin B (6) that were obtained in 4% and 5% overall yield, respectively. For that, we developed a bioinspired strategy of only seven steps (Figure 2B), which contrasts with the complex syntheses required for other ORPphilins.^{21–24}

Using the fluorescent properties conferred by their 3-hydroxy-flavone scaffold, we performed equilibrium and kinetic measurements by FRET between OSBP ORD tryptophans and (R) and (S) enantiomers of macarangin B (6). We showed that both bind the ORD domain of OSBP, albeit with distinct affinities: in the tens of nanomolar range for (R)-6 and in the submicromolar range for (S)-6 (Figure 2F). The emission of (R)-6 and (S)-6 in the visible spectrum enabled us to precisely define their intracellular distribution close to OSBP in the TGN region. Moreover, their accumulation in cells varied as a function of OSBP expression levels but not ORP4, indicating that (R)-6 and (S)-6 are selective toward OSBP (Figure 4A,B). In addition, (R)-6 had a stronger tendency to concentrate at the TGN and showed a more potent effect in recruiting OSBP at ER/TGN contact sites compared to (S)-6. *In silico* approaches further indicated that the binding site for (R)-6 and (S)-6 overlapped with the sterol-binding site into the hydrophobic cavity of the ORD. Most interestingly, molecular docking and MD simulations predicted that (R)-6, but not (S)-6, is able to adopt two different orientations within the ORD binding site (Figure 3A). Site-directed mutagenesis confirmed the importance of two residues, F440 and K577, in the interaction with macarangin B (6) enantiomers (Figure 4E,F).

Taken together, the structural, biochemical and cellular properties of macarangin B (6) presented here classify this molecule as a new ORPphilin. However, all ORPphilins

described so far show a similar pattern of sensitivity against the NCI 60 cancer cell lines and are highly cytotoxic for specific cell lines, such as glioblastoma.¹¹ By contrast, compounds (R)-6 and (S)-6 had a much lower cytotoxicity (Figure 5A), which did not correlate with their affinity for OSBP. These results sharply deviate from our recent findings on various SW derivatives, where a good parallel between K_i for OSBP and cytotoxicity on U-87 MG cells was observed, with the highest affinity for OSBP coinciding with maximum cytotoxicity.⁵¹ Moreover, whereas the absolute configuration of the HHX moiety of (R)- and (S)-6 influenced their affinity for OSBP, it had no impact on their cytotoxicity, which was both modest and similar. This result also differs from the data obtained for SWs where the (S) enantiomer was less cytotoxic than the (R) enantiomer.⁴⁰ The most likely explanation is that the previously described ORPphilins target other protein(s) that play a critical role in cell death, in addition to OSBP. In this respect, a cephalostatin–ritterazine hybrid compound was found to target the HSP70 isoform GRP78, leading to cell death by apoptosis.²⁰ Recent findings also showed that OSBP deficiency had little effect on OSW-1-induced cell death in Neuro2a cells.⁵² In fact, among ORPs, only ORP3, 4, 5, and 8 but not OSBP have been implicated in cell proliferation and tumor transformation.¹⁸ For example, ORP4 is involved in hematologic malignancies.⁵³ Importantly, our overexpression experiments suggest that neither (R)-6 nor (S)-6 could bind to ORP4, indicating a high specificity of these compounds for OSBP. As ORP4 is the target of the other ORPphilins but not of the SWs,¹⁷ these differences suggest that beyond OSBP and ORP4, other target(s) responsible for their cytotoxicity remain to be identified.

Many RNA viruses, like orthoflaviviruses, coopt the host lipid metabolic network to facilitate their replication. Notably, OSBP activity is hijacked by viruses to transport cholesterol in their replication organelles.^{25–27,29} Evidence suggests that targeting OSBP by inhibitors blocks viral infection,^{25,28,54} and this could be an attractive therapeutic approach to treat viral illnesses like Zika fever, yet lacking both vaccines and curative treatments.⁵⁵ Despite their good affinity for OSBP, ORPphilins are too cytotoxic to be used as antivirals. Various other non-natural OSBP inhibitors have been reported to have antiviral properties (Figure S7).^{27,28,30–32} Most of them were identified by chemical screening thanks to their antienterovirus activities. However, none is selective toward OSBP, as all of them target at least also ORP4. As ORP4 plays a role in cancer cell survival and proliferation, an OSBP-selective molecule such as (R)-6 is highly desirable for designing effective antiviral compounds. We showed that this compound had high anti-ZIKV activity (Figure 5B,C) and, owing to its low toxicity, a high selectivity index. (R)-6 also offers the advantage of being easy to modulate, making it a perfect hit for subsequent modifications.

CONCLUSIONS

Natural macarangin B (6), the ORPphilin with the simplest structure described so far, is also the most selective for OSBP. Its characteristics strongly question whether OSBP is the main target in the specific anticancer mechanism of ORPphilins. The extent to which OSBP is or is not involved in this mechanism remains to be defined. Importantly, (R)-6 allowed us also to validate OSBP as a promising anti-ZIKV target. This result is in line with the growing view that specifically targeting lipid metabolism pathways, in particular cholesterol metabolism, to interfere with orthoflavivirus infection should provide effective antiviral therapeutic avenues.⁵⁶

EXPERIMENTAL SECTION

Plant Material. The green fruits of *M. tanarius* were collected in June 2014 at A Luoi, Thua Thien Hue Province, Vietnam, and authenticated by N.T. Cuong and D.D. Cuong. A voucher specimen (VN-2371) has been deposited at the Herbarium of Institute of Ecology and Biological Resources of The Vietnam Academy of Science and Technology, Hanoi, Vietnam. ABS-CH Unique Identifier (UID): ABSCH-IRCC-VN-255602-1

Extraction and Isolation of Macarangin B (6). Dried fruits (3 kg) of *M. tanarius* were extracted with ethanol (3 × 10 L). The EtOH solution was evaporated to dryness under reduced pressure to give a crude extract. This extract was subjected to sequential liquid/liquid partitioning using water (1 L) and Et₂O (1 L) and CH₂Cl₂ (700 mL) to yield a CH₂Cl₂ extract (35 g) after concentration in vacuo at 40 °C. This CH₂Cl₂ extract (30 g) was subjected to silica gel column chromatography using a gradient of *n*-heptane–EtOAc–MeOH (4:6:0 to 0:8:2) of increasing polarity to afford eight fractions, FA1–FA8, according to their TLC profiles. Fraction FA6 (2.1 g) was subjected to silica gel column flash chromatography using a gradient of *n*-heptane–EtOAc (3:7 to 0:1) of increasing polarity to afford five fractions, FD1–FD5. Compound 6 (5 mg) was obtained by preparative reversed-phase HPLC (C18 column, Kromasil, 250 × 21.2 mm, 5 μm, CH₃CN–H₂O 45:55 or 55:65 + 0.1% formic acid at 21 mL/min) of fraction FD4 (103 mg). Macarangin B (6): pale yellow amorphous solid; $[\alpha]_D^{24}$ 0° (c 0.1, MeOH); UV–vis (MeOH) $\lambda(\epsilon)$ [nm (M^{−1} cm^{−1})] 363 (15 750); 269 (14 480); 204 (24 880); IR ν 824, 1054, 1267, 1439, 1517, 1664, 2921, 2970, 3990 cm^{−1}; HRESIMS m/z [M + H]⁺ 439.1757 (calcd for C₂₅H₂₇O₇⁺, 439.1751); ¹H NMR (500 MHz, CD₃OD) δ 8.06 (d, 2 H, *J* = 8.8 Hz), 6.90 (d, 2 H, *J* = 8.8 Hz), 6.50 (s, 1 H), 3.40 (dd, 1 H, *J* = 11.7, 4.1 Hz), 2.77 (dd, 1 H, *J* = 16.6, 5.1 Hz), 2.43 (dd, 1 H, *J* = 16.6, 13.0 Hz), 2.20 (m, 1 H), 1.87 (m, 1 H), 1.84 (m, 1 H), 1.67 (m, 1 H), 1.65 (dd, 2 H, *J* = 13.2, 5.2 Hz), 1.27 (s, 3 H), 1.12 (s, 3 H), 0.91 (s, 3 H) ppm; ¹³C NMR (125 MHz, CD₃OD) δ 173.9, 162.5, 160.3, 158.5, 155.2, 144.6, 138.4, 130.3 (2 C), 124.0, 116.5 (2 C), 108.4, 106.6, 94.8, 79.5, 78.9, 47.4, 39.8, 38.7, 29.2, 28.0, 20.1, 19.1, 15.0 ppm; see also Table S1.

Chemistry. All reagents and solvents for chemical synthesis were used as purchased from commercial suppliers or were purified/dried according to Armarego and Chai.⁵⁷ Optical rotations were measured at 20 °C on an Anton Paar MCP 300 polarimeter. UV spectra were recorded on a Varian Cary 100 UV–vis spectrophotometer. IR spectra were recorded on a PerkinElmer BX FT-IR spectrometer. 1D and 2D NMR spectra were recorded in CD₃OD or CD₃CN on Bruker 300, 500, or 700 MHz NMR instruments (Avance 300, 500 and 700). Chemical shifts (δ values) are given in parts per million (ppm), and multiplicity of signals are reported as follows: s, singlet; bs, broad singlet; d, doublet; t, triplet; q, quartet; dd, doublet of doublets; m, multiplet. High-resolution mass spectra were obtained on a Waters LCT Premier XE spectrometer in electrospray ionization mode by direct infusion of the purified compounds. Kromasil analytical and preparative C₁₈ columns (150 × 4.6 mm and 250 × 21.1 mm i.d.; 5 μm Thermo) were used for HPLC separation using a Waters autopurification system equipped with a sample manager (Waters 2767), a UV–vis diode array detector (190–600 nm, Waters 2996), and a PL-ELS 1000 ELSD Polymer Laboratory detector. All solvents and silica gel 60 (6–35 μm) were purchased from SDS (Messia sur Sorne, France), and

preparative and analytical TLC plates (Si gel 60 F254) were from Merck (Saint Quentin Fallavier, France). Prepacked GraceResolv silica cartridges were used for flash chromatography using a Teledyne Isco Combiflash Rf 200i. Natural and (R)- and (S)-**6** are >95% pure according to HPLC analysis performed on a Waters LCT Premier XE spectrometer.

6-(3,7-Dimethylocta-2,6-dien-1-yl)-5-hydroxy-3,7-is-(methoxymethoxy)-2-(4-(methoxymethoxy)phenyl)-4H-chromen-4-one (11). A mixture of kaempferol **9** (5.00 g, 17.47 mmol) and K_2CO_3 (29.00 g, 209.62 mmol, 12.0 equiv) in acetonitrile/DMSO 10:1 (260 mL) was heated at 40 °C for 1 h and cooled to room temperature. MOMCl (5.86 mL, 87.34 mmol, 5.0 equiv) was then added dropwise over 1 h and the resulting mixture was stirred at room temperature until completion of the reaction (TLC analysis). The reaction mixture was quenched with HCl 2 M (105 mL) and the product was extracted 3 times with EtOAc. The combined organic phases were washed with brine, dried over $MgSO_4$ and concentrated under reduced pressure. The crude mixture was purified by column chromatography on silica gel using heptane/EtOAc 95:5 to 0:100 + 1% of AcOH to obtain MOM-protected kaempferol as a pale-yellow solid (3.20 g, 7.65 mmol, 44%).

5-Hydroxy-3,7-bis(methoxymethoxy)-2-(4-(methoxymethoxy)phenyl)-4H-chromen-4-one. 1H NMR (300 MHz, CD_3CN) δ 12.55 (s, 1 H, OH), 8.04 (d, 2 H, J = 8.2 Hz), 7.17 (d, 2 H, J = 9.3 Hz), 6.66 (d, 1 H, J = 2.2 Hz), 6.40 (d, 1 H, J = 2.2 Hz), 5.26 (s, 2 H), 5.25 (s, 2 H), 5.12 (s, 2 H), 3.45 (s, 6 H), 3.19 (s, 3 H) ppm; ^{13}C NMR (75 MHz, CD_3CN) δ 179.7, 164.0, 162.7, 160.3, 157.8, 157.7, 136.5, 131.6, 124.7, 116.9, 107.2, 100.1, 98.8, 95.3, 95.2, 95.1, 58.0, 56.8, 56.6 ppm; IR ν 3095, 2924, 2828, 1595, 1493, 1147, 1066 cm^{-1} ; HRMS (ESI) m/z calculated for $C_{21}H_{23}O_9^+$ [$M + H$] $^+$: 419.1337, found: 419.1268.

A suspension of MOM-protected kaempferol (1.49 g, 3.57 mmol), $NaHCO_3$ (1.50 g, 17.85 mmol, 5.0 equiv) and BTMA- ICl_2 (1.30 g, 3.75 mmol, 1.05 equiv) in DCM/MeOH 2:1 (40 mL) was stirred under argon at room temperature in the dark for 1 h, until the reaction was completed (TLC analysis). The reaction was quenched carefully at 0 °C with 1 M HCl and neutralized to pH 5. The resulting mixture was extracted 3 times with a 2:1 solution of DCM and MeOH. The combined organic phases were dried over $MgSO_4$ and concentrated under reduced pressure. The crude iodinated intermediate (1.95 g) was directly engaged in the next step without further purification.

The preceding crude mixture (3.57 mmol) and geranyl boronic ester **10** (1.41 g, 5.35 mmol, 1.5 equiv) were solubilized in 45 mL of degassed THF/water (1:1) was added NaOH (357 mg, 8.92 mmol, 2.5 equiv) and $Pd(PPh_3)_4$ (111 mg, 0.07 mmol, 0.02 equiv).⁴⁶ The mixture was then heated at 100 °C under microwave irradiation for 4 h. The mixture was then filtrated on a pad of Celite, water was added and the product was extracted 3 times with EtOAc. The combined organic phases were washed with brine, dried over $MgSO_4$, filtrated and concentrated. The crude product was purified by column chromatography on silica gel using heptane/EtOAc 95:5 to 0:100 + 1% of AcOH to give **11** (E/Z 2:1) as a pale-yellow oil (1.40 g, 2.52 mmol, 71% for 2 steps from **1-1**). Compound **11**: IR ν 3070, 2959, 2910, 2829, 1654, 1606, 1587, 1243, 1151, 1055 cm^{-1} ; HRMS (ESI) m/z calculated for $C_{31}H_{39}O_9^+$ [$M + H$] $^+$: 555.2589, found: 555.2595. Compound (E)-**11**: 1H NMR (500 MHz, CD_3CN) δ 12.80 (s, 1 H, OH), 8.05 (d, 2 H, J = 9.6 Hz), 7.16 (dd, 2 H, J = 8.4 Hz), 6.73 (s, 1 H), 5.29 (s, 2 H), 5.26 (s, 2 H), 5.21 (t, 1 H, J = 8.4 Hz), 5.13 (s, 2 H), 5.05 (t, 1 H, J = 6.6 Hz), 3.45 (s, 6 H), 3.35

(d, 2 H, J = 8.4 Hz), 3.20 (s, 3 H), 2.27–2.22 (m, 1 H), 2.15–2.02 (m, 2 H), 1.99–1.94 (m, 1 H), 1.79 (s, 3 H), 1.64 (s, 3 H), 1.55 (s, 3 H) ppm; ^{13}C NMR (125 MHz, CD_3CN) δ = 179.8, 161.7, 160.4, 159.2, 157.7, 156.0, 136.7, 136.4, 132.2, 131.6 (2 C), 125.3, 125.0, 122.9, 117.0 (2 C), 113.8, 107.0, 98.9, 95.3, 95.2, 93.4, 58.1, 57.0, 56.7, 40.5, 27.5, 25.9, 22.2, 17.8, 16.4 ppm; compound (Z)-**11**: 1H NMR (500 MHz, CD_3CN) δ 12.82 (s, 1 H, OH), 8.05 (d, 2 H, J = 9.6 Hz), 7.16 (dd, 2 H, J = 8.4 Hz), 6.73 (s, 1 H), 5.29 (s, 2 H), 5.26 (s, 2 H), 5.21 (t, 1 H, J = 8.4 Hz), 5.13 (s, 2 H), 5.13 (t, 1 H, J = 6.6 Hz), 3.45 (s, 6 H), 3.35 (d, 2 H, J = 8.4 Hz), 3.20 (s, 3 H), 2.27–2.22 (m, 1 H), 2.15–2.02 (m, 2 H), 1.99–1.94 (m, 1 H), 1.69 (s, 3 H), 1.66 (s, 3 H), 1.64 (s, 3 H) ppm; ^{13}C NMR (125 MHz, CD_3CN) δ 179.8, 161.7, 160.4, 159.2, 157.7, 156.0, 136.8, 136.4, 132.4, 131.6 (2 C), 125.5, 125.0, 123.7, 117.0 (2 C), 114.9, 107.0, 98.9, 95.3, 95.2, 93.4, 58.1, 57.0, 56.7, 32.7, 27.5, 26.0, 23.6, 22.1, 17.9 ppm.

(R)- and (S)-**6-(5-(3,3-Dimethyloxiran-2-yl)-3-ethylpent-2-en-1-yl)-5-hydroxy-3,7-bis(methoxymethoxy)-2-(4-(methoxymethoxy)phenyl)-4H-chromen-4-one ((R)-13 and (S)-13).** To a solution of **11** in *t*-BuOH/water (2:1) were added K_2CO_3 (4.0 equiv), K_3FeCN_6 (2.8 equiv), (DHQ) $_2$ PHAL or (DHQD) $_2$ PHAL (0.04 equiv), OsO_4 (0.04 equiv) and methanesulfonamide (1.3 equiv). The reaction mixture was stirred at 0 °C for 16 h and quenched with a saturated aqueous solution of Na_2SO_3 . The product was then extracted with EtOAc (3 times). The combined organic phases were washed with brine, dried over $MgSO_4$, filtrated and concentrated under reduced pressure to give (S)-**12** (when (DHQ) $_2$ PHAL was used) or (R)-**12** (when (DHQD) $_2$ PHAL was used). (S)-**12** or (R)-**12** was directly engaged in the next step. Diol **12** was placed in a dry flask under argon and solubilized in anhydrous dichloromethane at 0 °C. Freshly distilled triethylamine (4.0 equiv) was added and the resulting solution was stirred at the same temperature for 30 min. Methanesulfonyl chloride (2.0 equiv) was then added and the mixture was stirred for 1 h. When the reaction was completed (TLC monitoring), DBU (5.0 equiv) was added and the mixture was stirred at 0 °C. After 3 h, the mixture was quenched with an aqueous solution of NH_4Cl and warmed to room temperature. The aqueous phase was decanted and the product was extracted 3 times with EtOAc. The combined organic phases were washed with water, dried with $MgSO_4$, filtrated and concentrated under reduced pressure. The product was purified by column chromatography on silica gel using heptane/EtOAc 95:5 to 0:100 + 1% of AcOH to obtain (R)-**13** or (S)-**13** as pale-yellow oils. Compound (R)-**13** (117 mg, 0.21 mmol) was obtained in 52% after 3 steps from **11** (220 mg, 0.40 mmol); HRMS (ESI) m/z calculated for $C_{31}H_{39}O_{10}^+$ [$M + H$] $^+$: 571.2538, found: 571.2516. Compound (S)-**13** (160 mg, 0.64 mmol) was obtained in 44% after 3 steps from **11** (355 mg, 0.64 mmol); HRMS (ESI) m/z calculated for $C_{31}H_{39}O_{10}^+$ [$M + H$] $^+$: 571.2538, found: 571.2525. Compound **13**: IR ν 3454, 2970, 2926, 1739, 1650, 1594, 1457, 1346, 1229, 1080, 1063, 988, 923 cm^{-1} ; (E)-**13**: 1H NMR (500 MHz, CD_3CN) δ 12.78 (s, 1 H, OH), 8.02 (d, 2 H, J = 8.3 Hz), 7.14 (dd, 2 H, J = 8.3 Hz), 6.69 (s, 1 H), 5.28 (s, 2 H), 5.25 (s, 3 H), 5.11 (s, 2 H), 3.44 (s, 6 H), 3.34 (d, 2 H, J = 6.9 Hz), 3.19 (s, 3 H), 2.58 (t, 1 H, J = 5.5 Hz), 2.13–2.02 (m, 2 H), 1.80 (s, 3 H), 1.66–1.45 (m, 2 H), 1.15 (s, 3 H), 1.14 (s, 3 H) ppm; ^{13}C NMR (125 MHz, CD_3CN) δ 179.6, 161.5, 160.2, 159.0, 157.5, 155.9, 136.6, 135.7, 131.5 (2 C), 124.8, 123.3, 116.9 (2 C), 113.5, 106.9, 98.8, 95.2, 95.1, 93.3, 64.5, 58.6, 58.0, 56.9, 56.6, 37.0, 28.1, 24.9, 22.2, 18.9, 16.3 ppm; (Z)-**13**: 1H NMR (500 MHz, CD_3CN) δ 12.80 (s, 1 H, H–OH), 8.02 (d, 2 H, J = 8.3 Hz), 7.14 (d, 2 H, J = 8.3 Hz),

6.69 (s, 1 H), 5.28 (s, 2 H), 5.25 (s, 3 H), 5.11 (s, 2 H), 3.44 (s, 6 H), 3.34 (d, 2 H, $J = 6.9$ Hz), 3.19 (s, 3 H), 2.58 (t, 1 H, $J = 5.5$ Hz), 2.13–2.02 (m, 2 H), 1.67 (s, 3 H), 1.66–1.45 (m, 2 H), 1.27 (s, 3 H), 1.26 (s, 3 H) ppm; ^{13}C NMR (125 MHz, CD_3CN) δ 179.6, 161.5, 160.2, 159.0, 157.5, 155.9, 136.6, 136.0, 131.5 (2 C), 124.8, 123.9, 116.9 (2 C), 113.5, 106.9, 98.8, 95.2, 95.1, 93.3, 64.6, 58.6, 58.0, 56.9, 56.6, 36.9, 28.3, 25.1, 22.0, 19.0, 16.3 ppm.

(7a*R*,9*r*,11a*R*)-9-Hydroxy-2,6-bis(methoxymethoxy)-3-(4-(methoxymethoxy)phenyl)-8,8,11a-trimethyl-7a,8,9,10,11,11a-hexahydro-1*H*,7*H*-pyrano[2,3-*c*]xanthen-1-one ((*R,R,R*)-14** i.e., (*R*)-**14**).** To a solution of compound (*R*)-**13** (89 mg, 0.16 mmol) in anhydrous dichloromethane (8 mL) under argon atmosphere at -78°C was added dropwise a 10% solution of $\text{BF}_3\cdot\text{OEt}_2$ in CH_2Cl_2 (0.03 mL, 0.23 mmol, 1.5 equiv) was added. The reaction mixture was stirred at -78°C for 30 min before being quenched with 1.5 mL of water. The mixture was warmed to room temperature and the product was extracted 3 times with dichloromethane. The combined organic phases were washed with water, dried over MgSO_4 and concentrated under reduced pressure. The crude product was purified by preparative TLC, using heptane/EtOAc 2:8 with 1% of AcOH to give (*R,R,R*)-**14** i.e. (*R*)-**14** (27 mg, 0.05 mmol, 30%) and (*R,S,R*)-**14** (5 mg, 0.01 mmol, 6%) as yellow oils. Compound (*R,R,R*)-**14**: $[\alpha]_{\text{D}}^{20} +83^\circ$ (c 1.0, MeOH); IR 3434, 2927, 1635, 1602, 1510, 1434, 1343, 1152, 1079, 989, 836 cm^{-1} ; ^1H NMR (500 MHz, CD_3CN) δ 8.02 (d, 2 H, $J = 8.4$ Hz), 7.15 (d, 2 H, $J = 8.4$ Hz), 6.72 (s, 1 H), 5.31 (m, 2 H), 5.25 (s, 2 H), 5.09 (q, 2 H, $J = 6.4$ Hz), 3.48 (s, 3 H), 3.45 (s, 6 H), 3.40–3.35 (m, 1 H), 3.18 (s, 3 H), 2.77 (dd, 1 H, $J = 15.6, 5.6$ Hz), 2.76 (s, 1 H), 2.44 (dd, 1 H, $J = 16.8, 14.6$ Hz), 2.07–2.02 (m, 1 H), 1.83–1.75 (m, 2 H), 1.67–1.58 (m, 2 H), 1.21 (s, 3 H), 1.07 (s, 3 H), 0.86 (s, 3 H) ppm; ^{13}C NMR (125 MHz, CD_3CN) δ 173.9, 160.0, 159.8, 157.8, 154.8, 153.9, 138.6, 131.2 (2 C), 125.5, 116.9 (2 C), 110.3, 109.4, 98.4, 95.5, 95.2, 94.3, 78.7, 78.0, 57.9, 57.0, 56.6, 46.5, 39.3, 38.6, 29.1, 27.7, 20.2, 18.9, 14.9 ppm; HRMS (ESI) m/z calculated for $\text{C}_{31}\text{H}_{39}\text{O}_{10}^+$ $[\text{M} + \text{H}]^+$: 571.2538, found: 571.2518. Compound (*R,S,R*)-**14**: $[\alpha]_{\text{D}}^{20} +12^\circ$ (c 1.0, MeOH); IR ν 3435, 2936, 1607, 1509, 1451, 1348, 1155, 1155, 1094, 842 cm^{-1} ; ^1H NMR (700 MHz, CD_3CN) δ 8.02 (d, 2 H, $J = 8.4$ Hz), 7.15 (d, 2 H, $J = 8.4$ Hz), 6.72 (s, 1 H), 5.31 (s, 2 H), 5.25 (s, 2 H), 5.09 (q, 2 H, $J = 6.4$ Hz), 3.48 (s, 3 H), 3.45 (s, 6 H), 3.38–3.33 (m, 1 H), 3.18 (s, 3 H), 2.80–76 (dd, 2 H, $J = 17.0, 5.1$ Hz), 2.69 (d, 1 H, OH, $J = 4.3$ Hz), 2.13 (m, 1 H), 2.07–2.01 (m, 1 H), 1.94 (m, 1 H), 1.89–1.83 (m, 1 H), 1.52–1.57 (m, 1 H), 1.23 (s, 3 H), 1.00 (s, 3 H), 0.60 (s, 3 H) ppm; ^{13}C NMR (125 MHz, CD_3CN) δ 173.9, 159.6, 159.4, 157.5, 156.1, 153.8, 138.4, 131.1 (2 C), 125.5, 116.8 (2 C), 110.2, 109.2, 98.2, 95.2, 95.1, 94.0, 77.5, 75.8, 57.8, 56.8, 56.5, 38.7, 37.7, 32.7, 27.6, 27.0, 25.7, 22.3, 18.6 ppm; HRMS (ESI) m/z calculated for $\text{C}_{31}\text{H}_{39}\text{O}_{10}^+$ $[\text{M} + \text{H}]^+$: 571.2538, found: 571.2528.

(7a*S*,9*s*,11a*S*)-9-Hydroxy-2,6-bis(methoxymethoxy)-3-(4-(methoxymethoxy)phenyl)-8,8,11a-trimethyl-7a,8,9,10,11,11a-hexahydro-1*H*,7*H*-pyrano[2,3-*c*]xanthen-1-one ((*S,S,S*)-14** i.e., (*S*)-**14**).** Same procedure as above starting from compound (*S*)-**13** (138 mg, 0.24 mmol) to give (*S,S,S*)-**14** i.e., (*S*)-**14** (44 mg, 0.08 mmol, 32%) and (*R,S,R*)-**14** (7 mg, 0.01 mmol, 5%) as yellow oils. Compound (*S*)-**14**: $[\alpha]_{\text{D}}^{20} -82^\circ$ (c 1.0, MeOH); HRMS (ESI) m/z calculated for $\text{C}_{31}\text{H}_{39}\text{O}_{10}^+$ $[\text{M} + \text{H}]^+$: 571.2538; found: 571.2532; Compound (*R,S,S*)-**14**: $[\alpha]_{\text{D}}^{20} -17^\circ$ (c 1.0, MeOH); HRMS (ESI) m/z calculated for $\text{C}_{31}\text{H}_{39}\text{O}_{10}^+$ $[\text{M} + \text{H}]^+$: 571.2538, found: 571.2565.

(*R,R,R*)-Macarangin B ((*R,R,R*)-6** i.e., (*R*)-**6**).** To a solution of compound (*R,R,R*)-**14** (8.5 mg, 0.01 mmol, 1.0 equiv) in methanol (0.5 mL) under argon atmosphere at 35°C was added of Dowex 50WX8 200–400 (47 mg, 0.2 mmol, 15.0 equiv). The mixture was stirred for 22 h at the same temperature. The resin was eliminated by filtration the filtrate was concentrated under reduced pressure to give pure (*R,R,R*)-**6** (6.5 mg, 0.01 mmol, 99%) as a pale yellow amorphous solid. Compound (*R,R,R*)-**6**: $[\alpha]_{\text{D}}^{20} +82^\circ$ (c 1.0, MeOH); ^1H and ^{13}C NMR spectra identical to that of natural macarangin B; HRMS (ESI) m/z calculated for $\text{C}_{25}\text{H}_{27}\text{O}_7^+$ $[\text{M} + \text{H}]^+$: 439.1778, found: 439.1751.

(*S,S,S*)-Macarangin B ((*S,S,S*)-6** i.e., (*S*)-**6**).** Same procedure as above starting from (*S,S,S*)-**14** (10 mg, 0.02 mmol) to give (*S,S,S*)-**6** (7 mg, 0.015 mmol, 91%) as a pale yellow amorphous solid. Compound (*S,S,S*)-**6**: $[\alpha]_{\text{D}}^{20} -91^\circ$ (c 1.0, MeOH); ^1H and ^{13}C NMR spectra identical to that of natural macarangin B; HRMS (ESI) m/z calculated for $\text{C}_{25}\text{H}_{27}\text{O}_7^+$ $[\text{M} + \text{H}]^+$: 439.1751; found: 439.1754.

Liposomes. Egg PC (1- α -phosphatidylcholine), liver PI (1- α -phosphatidylinositol), liver PE (1- α -phosphatidylethanolamine), brain PS (1- α -phosphatidylserine), and DNS-PE (1,2-dioleoyl-*sn*-glycero-3-phosphoethanolamine-*N*-(5-dimethylamino-1-naphthalenesulfonyl)) were purchased from Avanti Polar Lipids. Dehydroergosterol (DHE; ergosta-5,7,9(11),22-tetraen-3 β -ol) was from Sigma-Aldrich. The concentration of DHE in stock solution in methanol was determined by UV-spectroscopy using an extinction coefficient of 13,000 $\text{M}^{-1}\cdot\text{cm}^{-1}$. Lipids in chloroform were mixed at the desired molar ratio, and the solvent was removed in a rotary evaporator. The lipid film was hydrated in 50 mM HEPES pH 7.2, 120 mM potassium acetate (HK buffer) to give a suspension of large multilamellar liposomes. The suspension was then frozen in liquid nitrogen and thawed in a warm water bath five times. Liposomes were extruded through polycarbonate filters of 0.1 μm pore size using a mini-extruder (Avanti Polar Lipids). Unilamellar liposomes were stored in the dark and used within 2 days. ER-like liposomes contain: egg PC/brain PS (95/5 mol %) and Golgi-like liposomes contain: egg PC/liver PE/brain PS/liver PI/DNS-PE (63.5/19.5/10/2.5 mol %).

Sterol Transfer Assay. The human OSBP ORD fragment (401–807) with a C-terminal 6 \times His tag was expressed and purified from baculovirus-infected Sf9 cells as previously described.¹⁷ Golgi-like liposomes (63.3 μM total lipids) and ER-like liposomes supplemented with 18 mol % DHE (63.3 μM total lipids) were mixed in HKM buffer (HK buffer supplemented with 1 mM MgCl_2) in the presence of natural macarangin B (**6**) or OSW-1 (different stock concentration in DMSO, DMSO/buffer final ratio v/v 1/100), prior to the addition of OSBP ORD (100 nM final concentration). The sterol transport activity was monitored by FRET between DHE and DNS-PE, measured at 525/5 nm upon excitation at 310/1.5 nm in a Jasco FP-8300 spectrofluorimeter using a cylindrical quartz cuvette (600 μL) equilibrated at 37°C and equipped with a magnetic bar for continuous stirring.

Fluorescence Spectroscopy. (*R*)-**6** and (*S*)-**6** excitation (excitation 290–450/1 nm; emission 550/5 nm), emission (excitation 370/1 nm, emission 380–650/5 nm), or FRET (excitation 290/1 nm; emission 300–650/5 nm) spectra were carried out in a Jasco FP-8300 spectrofluorimeter using a cylindrical quartz cuvette (600 μL) equilibrated at 37°C and equipped with a magnetic bar for continuous stirring. Kinetics FRET measurements were performed with these settings:

excitation 290/1 nm; emission 550/5 nm. SW-G fluorescence spectroscopy was performed as previously described.¹⁷

Gel Filtration Assay. Gel filtration was performed on Sephadex G-25 NAP-5 columns (Cytiva) at room temperature. ORD (1 μ M) was incubated with (R)-6 or (S)-6 (500 nM) in 500 μ L HKM buffer supplemented with Thesit (0.02%) for 15 min. The sample was then loaded onto pre-equilibrated NAP-5 column and eluted by gravity flow, by sequentially adding 200 μ L of buffer to the column. The collected 200 μ L fractions were then analyzed for ORD (tryptophan) fluorescence (excitation 285/1 nm; emission 300–500/5 nm) and for (R)-6 or (S)-6 intrinsic fluorescence (excitation 370/2.5 nm; emission 400–650/10 nm) in a Jasco FP-8300 spectrofluorimeter using a Hellma 3 mm SUPRASIL quartz glass cell.

Docking Simulations. Docking simulations of cholesterol, SW-G, OSW-1, (R)-6 and (S)-6 were carried out on OSBP ORD (PDB ID: 7V62).⁴⁹ The SMILES IDs of the different compounds were converted into 3D structures with the NovoPro Lab server (<https://www.novoprolabs.com/tools/smiles2pdb>). For OSW-1, the lid of the ORD (residues 413 to 443) was removed before docking with PyMol 2.0, to avoid clashes between the compound and the lid. Correcting the clashes during minimization then allowed us to perform the simulation of OSW-1 with the full ORD. Docking simulations were run with AutoDock4.⁵⁸ We performed a rigid docking, testing 1000 poses with a population size of 300. Results were then clustered and ranked using an energy-based scoring. For each molecule, we determined the three best docking poses by examining the lowest energy poses in the biggest cluster. For (R)-6, two equivalent clusters were found, with “up” or “down” orientation of the HHX moiety. Thus, three poses were kept for each orientation.

Molecular Dynamics Simulations. The three chosen poses for cholesterol, SW-G, OSW-1, (R)-6 “up”, (R)-6 “down” and (S)-6 were used to perform all-atom molecular dynamics (MD) simulations of the compound in the ORD pocket. The topology of each compound was obtained in mol2 format with SwissParam.⁵⁹ For the protein, we used the CHARMM36 topology,^{60,61} adding COO[−] and NH₃⁺ at the termini. MD simulations were performed with GROMACS 2021.3,^{62,63} with the CHARMM36 force field. The systems were centered in a cubic box, at a minimum distance of 2 nm from box edges. Solvent molecules were added with the TIP3P water model configuration. Na⁺ and Cl[−] ions were added to neutralize the simulation box, at a concentration of 120 mM. The total number of atoms was around 185,000 for each system. Energy minimization was performed using the steepest descent minimization algorithm for the subsequent 50,000 steps. A step size of 0.01 nm was used during energy minimization. A cutoff distance of 1.2 nm was used for generating the neighbor list updated at every step. Long-range electrostatic interactions were calculated using the Particle Mesh Ewald summation method. Periodic boundary conditions and flexible water were used. A 200 ps NVT equilibration was performed, with a 2 ps time-step. The protein was restrained. Hydrogen bonds were constrained by the LINear Constraints Solver (LINCS) constraint algorithm. An NPT equilibration was performed similar to the NVT equilibration. During the production run, the V-rescale thermostat and Parrinello–Rahman barostat stabilized the temperature at 310.15 K and pressure at 1 bar, respectively. The simulations were performed for 500 ns with a time-step of 2 fs, with the two coupling groups Protein–Ligand and Water–Ions. Like equilibrations, the V-rescale thermostat, Parrinello–

Rahman barostat, 1.2 nm cutoff, PME method and LINCS algorithm were used. Coordinates were saved every 10 ps. MD analyzes of the RMSF of pocket residues, binding energies and the clustering were performed using GROMACS utilities. The first 10 ns were dismissed from RMSF calculations. RMSF in the presence of the different compounds were normalized to values obtained with cholesterol. Clustering was performed on each molecule over the three replicates, with the Gromos method. The cutoff was chosen so that approximately 20 clusters were found. The most representative structure of the first cluster was then kept for 3D visualization of the molecule in the pocket. The occurrence of hydrogen bonds (H-bonds) during the three replicates between each molecule and the ORD were calculated with the H-Bonds tool of the VMD software. H-bonds were defined with a maximal distance of 3.5 Å and a 30° angle. Python scripts were written to obtain the figures. Trajectories have been centered on the protein. Movies and images have been generated with VMD and PyMOL 2.0 software, respectively.

Cell Culture. hTERT-RPE1 cells (ATCC) were cultured in DMEM/F12 medium with glutaMAX (Gibco) containing 1% antibiotics (Zell Shield, Minerva Biolabs). A549, MCF7, PC3 (ATCC) and MDA MB 231 (DSMZ) cells were cultured in RPMI medium. U87-MG, HeLa and MRC-5 cells (ATCC) were cultured in DMEM. All cell lines growth media were supplemented with 10% fetal calf serum (FCS). Cells were incubated at 37 °C in a 5% CO₂ humidified atmosphere. Cells were passaged twice a week and used for testing after 2 weeks in culture. The absence of mycoplasma was measured using the MycoAlert Mycoplasma Detection Kit from Lonza.

Plasmid Generation and Transfection. OSBP and ORP4L were subcloned into pmCherry-N1 plasmids as described earlier.⁶⁴ Mutants were generated with the Quik-Change Lightning site-directed mutagenesis kit (Agilent Technologies). Generated plasmids were subjected to capillary sequencing prior to application to confirm that their sequences were correct. To transfect plasmid DNA, RPE-1 cells were nucleofected by Amaxa Nucleofector (Lonza) using Kit V, and cultured in Ibidi μ -Slide 8-well for 18 to 24 h, whereas A549 cells in 24-well plates were transfected using Lipofectamine 3000 (Invitrogen).

Microscopy. Confocal microscopy was performed with a Zeiss LSM 780 microscope operated with ZEN software using a Plan-Apochromat 63X/1.4 oil objective (Carl Zeiss). Each channel was acquired separately, by using sequential mode, to avoid cross-talk possibility between consecutive channels. For (R)-6 and (S)-6 imaging, a laser excitation at 405 nm was employed and fluorescence was detected in the channel 508–522 nm. Widefield microscopy was performed using an IX83 inverted microscope (Olympus) equipped with an iXon3 EMCCD camera (Andor) and an UPlanSApo 60X/1.35 oil objective (Olympus). SW-G was imaged as described previously.¹⁷ Immunofluorescence microscopy was carried out as previously described.¹⁷

Cell Viability Assay. Cells were seeded at 3000 cells/well density into white wall 96-well plates then treated on the following day with compounds. After 72 h treatment, cell viability was measured using CellTiter-Glo Luminescent Cell Viability Assay (Promega) and the luminescence was detected in a FLUOstar Omega microplate reader (BMG Labtech). Viability values of DMSO treated cells were considered as 100%, then surviving curves and IC50 values were determined using GraphPad Prism 7.0 software. Alternatively, a mitochondrial activity assay was used to assess compound toxicity in host

cells prior to antiviral evaluation. A549 cells (2×10^4 cells/well) plated into 96-well plate were treated with 2-fold dilutions of compounds ranging from 20 000 nM to 0.2 nM during 24, 48, or 72 h at 37 °C. Washed cells were incubated with 120 μ L, 5 mg/mL, of MTT (3-[4,5-dimethylthiazol-2-yl]-2,5-diphenyltetrazolium bromide) for 2 h. MTT solution was removed and formazan crystals were solubilized with 100 μ L of dimethyl sulfoxide (DMSO). Absorbance was measured at 570 nm with a background subtraction at 690 nm. The CC_{50} was determined using a nonlinear regression on Graphpad prism software.

Virology. A549 and Vero E6 cells were maintained at 37 °C and 5% CO_2 in MEM containing 4.5 g/L of D-glucose and supplemented with 5% FCS, 50 U/mL penicillin, 50 μ g/mL streptomycin, 2 mM L-glutamine, 0.5 μ g/mL fungizone and 1 mM sodium pyruvate. The clinical isolate PF-25013-18 of ZIKV (ZIKV-PF13) used in this study has been previously described.⁶⁵ ZIKV was grown in Vero cells and titrated by plaque forming assay. Antipan orthoflavivirus E monoclonal antibody 4G2 coupled with Alexa Fluor 594 was purchased from RD Biotech.

Antiviral Assay. A549 cells were infected with the epidemic strain of ZIKV at a multiplicity of infection (MOI) of 2 and simultaneously treated with various non cytotoxic concentrations of compounds. Twenty-four h pi, viral growth was titrated in the supernatant by plaque forming assay and the viral RNA copy number in ZIKV-A549 cells was measured by RT-qPCR. For RT-qPCR, total cellular RNA was extracted from cells with RNeasy kit (Qiagen) according to manufacturer's instructions. Reverse transcription was performed using a specific E protein reverse primer (5'-TTCACCTTGTTGGGC-3') and M-MLV reverse transcriptase (Life Technologies) at 42 °C for 50 min. Complementary DNA (cDNA) was amplified using a specific E protein forward primer (5'-GTCTTGGAACATGAGG-3'), the specific E reverse primer (described above) and 2X Absolute Blue qPCR SYBR Green Low ROX Master Mix (Thermo-Fisher) on a CFX96 Real-Time PCR Detection System (Bio-Rad). The CFX96 program was used to calculate the threshold cycle (Ct) for each well in the exponential phase of amplification. A synthetic gene coding for nucleotides 954 to 1306 of the MR766 strain (GenBank: LC002520) cloned in the pUC57 plasmid was used as template to generate a standard curve, which then served to make absolute quantitation of intracellular viral RNA. Viral progeny production was titrated and determined by a plaque-forming assay. Vero A549 cells were seeded in 24 well-plates at a density of 7×10^4 cells/well. The next day, cells were inoculated with 200 μ L of 10-fold dilutions of cell-infected supernatants. After 2 h of incubation at 37 °C, 300 μ L of MEM culture medium containing 5% FCS and 1% carboxymethylcellulose (Sigma-Aldrich) were added and infected cells were further incubated for 96 h at 37 °C. The medium was then removed and cells were washed twice with PBS, fixed with PFA 3.7%, and stained with 1% crystal violet (Sigma-Aldrich) diluted in 20% ethanol. Plaques were counted and represented as plaque-forming unit per mL (PFU/mL). For transfection experiments, A549 cells expressing OSBP or ORP4L-mCherry for 18 h were infected with Zika virus and simultaneously treated with compounds, or washed twice with PBS, trypsinized, fixed with PFA 3.7% for 15 min, and subjected to flow cytometric analysis for quantification of mCherry positive cells, by using a CytoFLEX flow cytometer (Beckman Coulter). Results were analyzed using CytExpert software.

■ ASSOCIATED CONTENT

Supporting Information

The Supporting Information is available free of charge at <https://pubs.acs.org/doi/10.1021/acs.jmedchem.4c01705>.

Supplementary figures, characterization of natural macarangenin B (6), raw NMR data, analytical data for all compounds (PDF)

MD simulation (500 ns) of (R)-6 “up” in OSBP ORD domain. The transient formation of H-bonds is shown by blue dashed lines. Residue F440 (pink) is the most frequently involved in H-bonding over time (AVI)

MD simulation (500 ns) of (R)-6 “down” in OSBP ORD domain. The transient formation of H-bonds is shown by blue dashed lines. Residue K577 (pink) is the most frequently involved in H-bonding over time. (AVI)

MD simulation (500 ns) of (S)-6 in OSBP ORD domain. The transient formation of H-bonds is shown by blue dashed lines. Residue K577 (pink) is the most frequently involved in H-bonding over time (AVI)

Molecular formula strings (ZIP)

■ AUTHOR INFORMATION

Corresponding Authors

Bruno Mesmin – Inserm, CNRS, Institut de Pharmacologie Moléculaire et Cellulaire, Université Côte d'Azur, Valbonne 06560, France; orcid.org/0000-0002-5437-3246; Email: mesmin@ipmc.cnrs.fr

Fanny Roussi – CNRS, Institut de Chimie des Substances Naturelles, Université Paris-Saclay, Gif-sur-Yvette 91198, France; orcid.org/0000-0002-5941-9901; Email: fanny.roussi@cnrs.fr

Authors

Gwenaëlle Jézéquel – CNRS, Institut de Chimie des Substances Naturelles, Université Paris-Saclay, Gif-sur-Yvette 91198, France

Zoé Grimanelli – Inserm, CNRS, Institut de Pharmacologie Moléculaire et Cellulaire, Université Côte d'Azur, Valbonne 06560, France; orcid.org/0009-0009-7495-285X

Carole Guimard – CNRS, Institut de Chimie des Substances Naturelles, Université Paris-Saclay, Gif-sur-Yvette 91198, France

Joëlle Bigay – Inserm, CNRS, Institut de Pharmacologie Moléculaire et Cellulaire, Université Côte d'Azur, Valbonne 06560, France

Juliano Haddad – Inserm U1187, CNRS UMR 9192, IRD UMR 249, Unité Mixte Processus Infectieux en Milieu Insulaire Tropical, Plateforme Technologique CYROI, Université de la Réunion, Sainte Clotilde 94791, France

Jérôme Bignon – CNRS, Institut de Chimie des Substances Naturelles, Université Paris-Saclay, Gif-sur-Yvette 91198, France

Cécile Apel – CNRS, Institut de Chimie des Substances Naturelles, Université Paris-Saclay, Gif-sur-Yvette 91198, France; orcid.org/0000-0003-3785-9620

Vincent Steinmetz – CNRS, Institut de Chimie des Substances Naturelles, Université Paris-Saclay, Gif-sur-Yvette 91198, France

Laurie Askenatzis – CNRS, Institut de Chimie des Substances Naturelles, Université Paris-Saclay, Gif-sur-Yvette 91198, France

Hélène Levaïque – CNRS, Institut de Chimie des Substances Naturelles, Université Paris-Saclay, Gif-sur-Yvette 91198, France

Clara Pradelli – Inserm, CNRS, Institut de Pharmacologie Moléculaire et Cellulaire, Université Côte d'Azur, Valbonne 06560, France

Van Cuong Pham – Institute of Marine Biochemistry, Vietnam Academy of Science and Technology, Hanoi 10000, Vietnam

Doan T. M. Huong – Institute of Marine Biochemistry, Vietnam Academy of Science and Technology, Hanoi 10000, Vietnam

Marc Litaudon – CNRS, Institut de Chimie des Substances Naturelles, Université Paris-Saclay, Gif-sur-Yvette 91198, France; orcid.org/0000-0002-0877-8234

Romain Gautier – Inserm, CNRS, Institut de Pharmacologie Moléculaire et Cellulaire, Université Côte d'Azur, Valbonne 06560, France; orcid.org/0000-0001-6678-132X

Chaker El Kalamouni – Inserm U1187, CNRS UMR 9192, IRD UMR 249, Unité Mixte Processus Infectieux en Milieu Insulaire Tropical, Plateforme Technologique CYROI, Université de la Réunion, Sainte Clotilde 94791, France; orcid.org/0000-0003-4673-6614

Bruno Antonny – Inserm, CNRS, Institut de Pharmacologie Moléculaire et Cellulaire, Université Côte d'Azur, Valbonne 06560, France

Sandy Desrat – CNRS, Institut de Chimie des Substances Naturelles, Université Paris-Saclay, Gif-sur-Yvette 91198, France; orcid.org/0000-0002-6544-9242

Complete contact information is available at:

<https://pubs.acs.org/10.1021/acs.jmedchem.4c01705>

Funding

This work was supported by the CNRS, Inserm, the Agence Nationale de la Recherche (ANR-21-CE13-0021-01), the ERC (Synergy #856404), two “Investissement d'Avenir” grants managed by Agence Nationale de la Recherche (UPSaclay ref CDE-2019-002288/IRE 2019-083 and CEBA, ANR-10-LABX-25-01), the “Investments for the Future” program LABEX SIGNALIFE (ANR-11-LABX-0028-01), a maturation program grant managed by the SATT Paris-Saclay (CM2017-0045), and the PHYTODENGUE program (Région Réunion N° SYNERGIE: RE0028005). This work benefited from computing and storage resources provided by GENCI at IDRIS on V100 and A100 partitions of the supercomputer Jean Zay (grants AD010714001 and A0150714646). G.J. and C.G. were supported by a PhD fellowship from the Université Paris Saclay (ED ITFA). Z.G. was supported by the Polytech Nice Sophia (Université Côte d'Azur) PhD fellowship program.

Notes

The authors declare no competing financial interest.

ACKNOWLEDGMENTS

We thank A. Patel and S. Abélanet (IPMC, Valbonne) for invaluable technical assistance; D. Lévy (Institut Curie, Paris), F. Alpy (IGBMC, Illkirch), C. Etchebest (Université Paris Cité) and P. Desprès (Université de la Réunion) for discussions, and all members of the Roussi and Antonny laboratories for their insights. We thank the IPMC Imaging and Cytometry facility, part of the MICA platform (GIS IBISA).

ABBREVIATIONS

DHE, dehydroergosterol; ER, endoplasmic reticulum; HHX, hexahydroxanthene; MD, molecular dynamics; ORD, OSBP-

related domain; ORP, OSBP-related protein; OSBP, oxysterol-binding protein; PI(4)P, phosphatidylinositol-4-phosphate; SW, schweinfurthin; TGN, trans-Golgi network; ZIKV, Zika virus

REFERENCES

- (1) Lautié, E.; Russo, O.; Ducrot, P.; Boutin, J. A. Unraveling Plant Natural Chemical Diversity for Drug Discovery Purposes. *Front. Pharmacol.* **2020**, *11*, 397.
- (2) Rodrigues, T.; Reker, D.; Schneider, P.; Schneider, G. Counting on Natural Products for Drug Design. *Nat. Chem.* **2016**, *8* (6), 531–541.
- (3) Lachance, H.; Wetzel, S.; Kumar, K.; Waldmann, H. Charting, Navigating, and Populating Natural Product Chemical Space for Drug Discovery. *J. Med. Chem.* **2012**, *55* (13), 5989–6001.
- (4) Rosén, J.; Gottfries, J.; Muresan, S.; Backlund, A.; Oprea, T. I. Novel Chemical Space Exploration via Natural Products. *J. Med. Chem.* **2009**, *52* (7), 1953–1962.
- (5) Pettit, G. R.; Inoue, M.; Kamano, Y.; Herald, D. L.; Arm, C.; Dufresne, C.; Christie, N. D.; Schmidt, J. M.; Doubek, D. L.; Krupa, T. S. Antineoplastic Agents. 147. Isolation and Structure of the Powerful Cell Growth Inhibitor Cephalostatin 1. *J. Am. Chem. Soc.* **1988**, *110* (6), 2006–2007.
- (6) Kubo, S.; Mimaki, Y.; Terao, M.; Sashida, Y.; Nikaido, T.; Ohmoto, T. Acylated Cholestane Glycosides from the Bulbs of *Ornithogalum Saundersiae*. *Phytochemistry* **1992**, *31* (11), 3969–3973.
- (7) Fukuzawa, S.; Matsunaga, S.; Fusetani, N. Isolation and Structure Elucidation of Ritterazines B and C, Highly Cytotoxic Dimeric Steroidal Alkaloids, from the Tunicate *Ritterella Tokioka*. *J. Org. Chem.* **1995**, *60* (3), 608–614.
- (8) McCormick, J. L.; McKee, T. C.; Cardellina, J. H.; Leid, M.; Boyd, M. R. Cytotoxic Triterpenes from a Marine Sponge, *Stelletta* Sp. *J. Nat. Prod.* **1996**, *59* (11), 1047–1050.
- (9) Koubek, E. J.; Weissenrieder, J. S.; Neighbors, J. D.; Hohl, R. J. Schweinfurthins: Lipid Modulators with Promising Anticancer Activity. *Lipids* **2018**, *53* (8), 767–784.
- (10) Rabow, A. A.; Shoemaker, R. H.; Sausville, E. A.; Covell, D. G. Mining the National Cancer Institute's Tumor-Screening Database: Identification of Compounds with Similar Cellular Activities. *J. Med. Chem.* **2002**, *45* (4), 818–840.
- (11) Burgett, A. W. G.; Poulsen, T. B.; Wangkanont, K.; Anderson, D. R.; Kikuchi, C.; Shimada, K.; Okubo, S.; Fortner, K. C.; Mimaki, Y.; Kuroda, M. Natural Products Reveal Cancer Cell Dependence on Oxysterol-Binding Proteins. *Nat. Chem. Biol.* **2011**, *7* (9), 639–647.
- (12) Wong, L. H.; Gatta, A. T.; Levine, T. P. Lipid Transfer Proteins: The Lipid Commute via Shuttles, Bridges and Tubes. *Nat. Rev. Mol. Cell Biol.* **2019**, *20* (2), 85–101.
- (13) Delfosse, V.; Bourguet, W.; Drin, G. Structural and Functional Specialization of OSBP-Related Proteins. *Contact* **2020**, *3*, 251525642094662.
- (14) Mesmin, B.; Bigay, J.; Moser von Filseck, J.; Lacas-Gervais, S.; Drin, G.; Antonny, B. A Four-Step Cycle Driven by PI(4)P Hydrolysis Directs Sterol/PI(4)P Exchange by the ER-Golgi Tether OSBP. *Cell* **2013**, *155* (4), 830–843.
- (15) Subra, M.; Antonny, B.; Mesmin, B. New Insights into the OSBP–VAP Cycle. *Curr. Opin. Cell Biol.* **2023**, *82*, 102172.
- (16) Mesmin, B.; Bigay, J.; Polidori, J.; Jamecna, D.; Lacas-Gervais, S.; Antonny, B. Sterol Transfer, PI4P Consumption, and Control of Membrane Lipid Order by Endogenous OSBP. *Embo J.* **2017**, *36* (21), 3156–3174.
- (17) Péresse, T.; Kovacs, D.; Subra, M.; Bigay, J.; Tsai, M.-C.; Polidori, J.; Gautier, R.; Desrat, S.; Fleuriet, L.; Debayle, D. Molecular and Cellular Dissection of the Oxysterol-Binding Protein Cycle through a Fluorescent Inhibitor. *J. Biol. Chem.* **2020**, *295* (13), 4277–4288.
- (18) Olkkonen, V. M. The Emerging Roles of OSBP-Related Proteins in Cancer: Impacts through Phosphoinositide Metabolism and Protein–Protein Interactions. *Biochem. Pharmacol.* **2022**, *196*, 114455.

- (19) Zhong, W.; Lin, W.; Yang, Y.; Chen, D.; Cao, X.; Xu, M.; Pan, G.; Chen, H.; Zheng, J.; Feng, X. An Acquired Phosphatidylinositol 4-Phosphate Transport Initiates T-Cell Deterioration and Leukemogenesis. *Nat. Commun.* **2022**, *13* (1), 4390.
- (20) Ambrose, A. J.; Santos, E. A.; Jimenez, P. C.; Rocha, D. D.; Wilke, D. V.; Beuzer, P.; Axelrod, J.; Kanduluru, A. K.; Fuchs, P. L.; Cang, H.; Costa-Lotufo, L. V. Ritterostatin G N I N, a Cephalostatin–Ritterazine Bis-steroidal Pyrazine Hybrid, Selectively Targets GRP78. *ChemBiochem* **2017**, *18* (6), 506–510.
- (21) Boyko, Y. D.; Huck, C. J.; Sarlah, D. Total Synthesis of Isomalabaricane Triterpenoids. *J. Am. Chem. Soc.* **2019**, *141* (36), 14131–14135.
- (22) Nakayama, Y.; Maser, M. R.; Okita, T.; Dubrovskiy, A. V.; Campbell, T. L.; Reisman, S. E. Total Synthesis of Ritterazine B. *J. Am. Chem. Soc.* **2021**, *143* (11), 4187–4192.
- (23) Tang, Y.; Li, N.; Duan, J.; Tao, W. Structure, Bioactivity, and Chemical Synthesis of OSW-1 and Other Steroidal Glycosides in the Genus *Ornithogalum*. *Chem. Rev.* **2013**, *113* (7), 5480–5514.
- (24) Harmalkar, D. S.; Mali, J. R.; Sivaraman, A.; Choi, Y.; Lee, K. Schweinfurthins A–Q: Isolation, Synthesis, and Biochemical Properties. *RSC Adv.* **2018**, *8* (38), 21191–21209.
- (25) Wang, H.; Perry, J. W.; Lauring, A. S.; Neddermann, P.; Francesco, R. D.; Tai, A. W. Oxysterol-Binding Protein Is a Phosphatidylinositol 4-Kinase Effector Required for HCV Replication Membrane Integrity and Cholesterol Trafficking. *Gastroenterology* **2014**, *146* (5), 1373–1385.e11.
- (26) Meutiawati, F.; Bezemer, B.; Strating, J. R. P. M.; Overheul, G. J.; Žusinaite, E.; Kuppeveld, F. J. M. V.; Cleef, K. W. R. V.; Rij, R. P. V. Posaconazole Inhibits Dengue Virus Replication by Targeting Oxysterol-Binding Protein. *Antivir. Res.* **2018**, *157*, 68–79.
- (27) Strating, J. R. P. M.; van der Linden, L.; Albuilescu, L.; Bigay, J.; Arita, M.; Delang, L.; Leyssen, P.; van der Schaar, H. M.; Lanke, K. H. W.; Thibaut, H. J. Itraconazole Inhibits Enterovirus Replication by Targeting the Oxysterol-Binding Protein. *Cell Rep.* **2015**, *10* (4), 600–615.
- (28) Arita, M.; Kojima, H.; Nagano, T.; Okabe, T.; Wakita, T.; Shimizu, H. Oxysterol-Binding Protein Family I Is the Target of Minor Enviroxime-Like Compounds. *J. Virol.* **2013**, *87* (8), 4252–4260.
- (29) Strating, J. R.; Kuppeveld, F. J. V. Viral Rewiring of Cellular Lipid Metabolism to Create Membranous Replication Compartments. *Curr. Opin. Cell Biol.* **2017**, *47*, 24–33.
- (30) De Palma, A. M.; Thibaut, H. J.; Linden, L. V. D.; Lanke, K.; Heggermont, W.; Ireland, S.; Andrews, R.; Arimilli, M.; Al-Tel, T. H.; Clercq, E. D.; van Kuppeveld, F. Mutations in the Nonstructural Protein 3A Confer Resistance to the Novel Enterovirus Replication Inhibitor TTP-8307. *Antimicrob. Agents. Chemo.* **2009**, *53* (5), 1850–1857.
- (31) Arita, M.; Takebe, Y.; Wakita, T.; Shimizu, H. A Bifunctional Anti-Enterovirus Compound That Inhibits Replication and the Early Stage of Enterovirus 71 Infection. *J. Gen. Virol.* **2010**, *91* (11), 2734–2744.
- (32) Gao, Q.; Yuan, S.; Zhang, C.; Wang, Y.; Wang, Y.; He, G.; Zhang, S.; Altmeyer, R.; Zou, G. Discovery of Itraconazole with Broad-Spectrum In Vitro Antienterovirus Activity That Targets Nonstructural Protein 3A. *Antimicrob. Agents Chemother.* **2015**, *59* (5), 2654–2665.
- (33) Allard, P.-M.; Péresse, T.; Bisson, J.; Gindro, K.; Marcourt, L.; Pham, V. C.; Roussi, F.; Litaudon, M.; Wolfender, J.-L. Integration of Molecular Networking and In-Silico MS/MS Fragmentation for Natural Products Dereplication. *Anal. Chem.* **2016**, *88* (6), 3317–3323.
- (34) Péresse, T.; Jézéquel, G.; Allard, P.-M.; Pham, V.-C.; Huong, D. T. M.; Blanchard, F.; Bignon, J.; Lévaïque, H.; Wolfender, J.-L.; Litaudon, M. Cytotoxic Prenylated Stilbenes Isolated from *Macaranga Tanarius*. *J. Nat. Prod.* **2017**, *80* (10), 2684–2691.
- (35) Péresse, T.; Elie, N.; Touboul, D.; Pham, V.-C.; Dumontet, V.; Roussi, F.; Litaudon, M.; Brunelle, A. Dual Beam Depth Profiling and Imaging with Argon and Bismuth Clusters of Prenylated Stilbenes on Glandular Trichomes of *Macaranga Vedeliana*. *Anal. Chem.* **2017**, *89* (17), 9247–9252.
- (36) Alseekh, S.; de Souza, L. P.; Benina, M.; Fernie, A. R. The Style and Substance of Plant Flavonoid Decoration; towards Defining Both Structure and Function. *Phytochemistry* **2020**, *174*, 112347.
- (37) Yang, X.; Jiang, Y.; Yang, J.; He, J.; Sun, J.; Chen, F.; Zhang, M.; Yang, B. Prenylated Flavonoids, Promising Nutraceuticals with Impressive Biological Activities. *Trends Food Sci. Technol.* **2015**, *44* (1), 93–104.
- (38) Huang, Y.-C.; Hwang, T.-L.; Chang, C.-S.; Yang, Y.-L.; Shen, C.-N.; Liao, W.-Y.; Chen, S.-C.; Liaw, C.-C. Anti-Inflammatory Flavonoids from the Rhizomes of *Helminthostachys Zeylanica*. *J. Nat. Prod.* **2009**, *72* (7), 1273–1278.
- (39) Huang, Y.-L.; Yeh, P.-Y.; Shen, C.-C.; Chen, C.-C. Antioxidant Flavonoids from the Rhizomes of *Helminthostachys Zeylanica*. *Phytochemistry* **2003**, *64* (7), 1277–1283.
- (40) Mente, N. R.; Wiemer, A. J.; Neighbors, J. D.; Beutler, J. A.; Hohle, R. J.; Wiemer, D. F. Total Synthesis of (R,R,R)- and (S,S,S)-Schweinfurthin F: Differences of Bioactivity in the Enantiomeric Series. *Bioorg. Med. Chem. Lett.* **2007**, *17* (4), 911–915.
- (41) Barrett, A.; Ma, T.-K.; Mies, T. Recent Developments in Polyene Cyclizations and Their Applications in Natural Product Synthesis. *Synthesis* **2019**, *51* (1), 67–82.
- (42) Hnawia, E.; Thoison, O.; Guéritte-Voegelein, F.; Bourret, D.; Sévenet, T. A Geranyl Substituted Flavonol from *Macaranga Vedeliana*. *Phytochemistry* **1990**, *29* (7), 2367–2368.
- (43) Basabe, P.; Román, M. D.; Diez, D.; Marcos, I.; Bodero, O.; Blanco, A.; Mollinedo, F.; Urones, J. Synthesis of Isoprenyl Flavonoids: (+)-Denticulaflavonol, Macarangin, and Isomacarangin. *Synlett* **2008**, *2008* (8), 1149–1152.
- (44) Quintin, J.; Lewin, G. Regioselective 6-Iodination of 5,7-Dioxygenated Flavones by Benzyltrimethylammonium Dichloroiodate. *Tetrahedron Lett.* **2004**, *45* (18), 3635–3638.
- (45) Lu, K.; Chu, J.; Wang, H.; Fu, X.; Quan, D.; Ding, H.; Yao, Q.; Yu, P. Regioselective Iodination of Flavonoids by N-Iodosuccinimide under Neutral Conditions. *Tetrahedron Lett.* **2013**, *54* (47), 6345–6348.
- (46) Dutheuil, G.; Selander, N.; Szabó, K.; Aggarwal, V. Direct Synthesis of Functionalized Allylic Boronic Esters from Allylic Alcohols and Inexpensive Reagents and Catalysts. *Synthesis* **2008**, *2008* (14), 2293–2297.
- (47) Monago-Maraña, O.; Durán-Merás, I.; Galeano-Díaz, T.; Peña, A. M. D. L. Fluorescence Properties of Flavonoid Compounds. Quantification in Paprika Samples Using Spectrofluorimetry Coupled to Second Order Chemometric Tools. *Food Chem.* **2016**, *196*, 1058–1065.
- (48) Höfener, S.; Kooijman, P. C.; Groen, J.; Ariese, F.; Visscher, L. Fluorescence Behavior of (Selected) Flavonols: A Combined Experimental and Computational Study. *Phys. Chem. Chem. Phys.* **2013**, *15* (30), 12572–12581.
- (49) Kobayashi, J.; Arita, M.; Sakai, S.; Kojima, H.; Senda, M.; Senda, T.; Hanada, K.; Kato, R. Ligand Recognition by the Lipid Transfer Domain of Human OSBP Is Important for Enterovirus Replication. *ACS Infect. Dis.* **2022**, *8*, 1161.
- (50) Albuilescu, L.; Strating, J. R. P. M.; Thibaut, H. J.; Linden, L. V. D.; Shair, M. D.; Neyts, J.; van Kuppeveld, F. J. M. Broad-Range Inhibition of Enterovirus Replication by OSW-1, a Natural Compound Targeting OSBP. *Antivir. Res.* **2015**, *117*, 110–114.
- (51) Jézéquel, G.; Rampal, C.; Guimard, C.; Kovacs, D.; Polidori, J.; Bigay, J.; Bignon, J.; Askenatzis, L.; Litaudon, M.; Pham, V.-C. Structure-Based Design of a Lead Compound Derived from Natural Schweinfurthins with Antitumor Properties That Target Oxysterol-Binding Protein. *J. Med. Chem.* **2023**, *66* (20), 14208–14220.
- (52) Oh-Hashi, K.; Nakamura, H.; Ogawa, H.; Hirata, Y.; Sakurai, K. Elucidation of OSW-1-Induced Stress Responses in Neuro2a Cells. *J. Mol. Sci.* **2023**, *24* (6), 5787.
- (53) Du, X.; Turner, N.; Yang, H. The Role of Oxysterol-Binding Protein and Its Related Proteins in Cancer. *Semin. Cell. Dev. Biol.* **2018**, *81*, 149–153.
- (54) Roberts, B. L.; Severance, Z. C.; Bensen, R. C.; Le, A. T.; Malinky, C. A.; Mettenbrink, E. M.; Nuñez, J. I.; Reddig, W. J.; Blewett, E. L.;

Burgett, A. W. G. Differing Activities of Oxysterol-Binding Protein (OSBP) Targeting Anti-Viral Compounds. *Antiviral Res.* **2019**, *170*, 104548.

(55) Pierson, T. C.; Diamond, M. S. The Continued Threat of Emerging Flaviviruses. *Nat. Microbiol.* **2020**, *5* (6), 796–812.

(56) Pombo, J. P.; Sanyal, S. Perturbation of Intracellular Cholesterol and Fatty Acid Homeostasis During Flavivirus Infections. *Front. Immunol.* **2018**, *9*, 1276.

(57) Armarego, W.; Chai, C. *Purification of Laboratory Chemicals*, 7th ed.; Elsevier, 2013.

(58) Morris, G. M.; Huey, R.; Lindstrom, W.; Sanner, M. F.; Belew, R. K.; Goodsell, D. S.; Olson, A. J. AutoDock4 and AutoDockTools4: Automated Docking with Selective Receptor Flexibility. *J. Comput. Chem.* **2009**, *30* (16), 2785–2791.

(59) Zoete, V.; Cuendet, M. A.; Grosdidier, A.; Michielin, O. SwissParam: A Fast Force Field Generation Tool for Small Organic Molecules. *J. Comput. Chem.* **2011**, *32* (11), 2359–2368.

(60) Brooks, B. R.; Brooks, C. L.; Mackerell, A. D.; Nilsson, L.; Petrella, R. J.; Roux, B.; Won, Y.; Archontis, G.; Bartels, C.; Boresch, S. CHARMM: The Biomolecular Simulation Program. *J. Comput. Chem.* **2009**, *30* (10), 1545–1614.

(61) Huang, J.; MacKerell, A. D. CHARMM36 All-atom Additive Protein Force Field: Validation Based on Comparison to NMR Data. *J. Comput. Chem.* **2013**, *34* (25), 2135–2145.

(62) Abraham, M. J.; Murtola, T.; Schulz, R.; Páll, S.; Smith, J. C.; Hess, B.; Lindahl, E. GROMACS: High Performance Molecular Simulations through Multi-Level Parallelism from Laptops to Supercomputers. *SoftwareX* **2015**, *1*, 19–25.

(63) Bekker, H.; Berendsen, H.; Dijkstra, E.; Achterop, S.; Drunen, R.; Spoel, D. V. D.; Sijbers, A.; Keegstra, H.; B, R.; Renardus, M. Gromacs: A Parallel Computer for Molecular Dynamics Simulations *4th international conference on computational physics* World Scientific Publishing 1993 92252–256

(64) Jamecna, D.; Polidori, J.; Mesmin, B.; Dezi, M.; Levy, D.; Bigay, J.; Antonny, B. An Intrinsically Disordered Region in OSBP Acts as an Entropic Barrier to Control Protein Dynamics and Orientation at Membrane Contact Sites. *Dev. Cell* **2019**, *49* (2), 220–234.e8.

(65) Gadea, G.; Bos, S.; Krejbich-Trotot, P.; Clain, E.; Viranaicken, W.; El-Kalamouni, C.; Mavingui, P.; Desprès, P. A Robust Method for the Rapid Generation of Recombinant Zika Virus Expressing the GFP Reporter Gene. *Virology* **2016**, *497*, 157–162.